

Hertzsprung gap stars in nearby galaxies and the Quest for Luminous Red Novae Progenitors[★]

Hugo Tranin^{1,2,3}, Nadejda Blagorodnova^{1,2,3}, Viraj Karambelkar⁴, Paul Groot⁵, Steven Bloemen⁵, Paul Vreeswijk⁵, Daniëlle Pieterse⁵, and Jan van Roestel⁶

¹ Institut de Ciències del Cosmos (ICCUB), Universitat de Barcelona (UB), c. Martí i Franquès, 1, 08028, Barcelona, Spain e-mail: hugo.tranin@irap.omp.eu

² Departament de Física Quàntica i Astrofísica (FQA), Universitat de Barcelona (UB), c. Martí i Franquès, 1, 08028, Barcelona, Spain

³ Institut d'Estudis Espacials de Catalunya (IEEC), c. Gran Capità, 2-4, 08034, Barcelona, Spain

⁴ Cahill Center for Astrophysics, California Institute of Technology, Pasadena, CA 91125, USA

⁵ Department of Astrophysics/IMAPP, Radboud University, PO Box 9010, 6500 GL Nijmegen, The Netherlands

⁶ Anton Pannekoek Institute for Astronomy, University of Amsterdam, 1090 GE Amsterdam, The Netherlands

ABSTRACT

Context. After the main sequence phase, stars more massive than $2.5 M_{\odot}$ rapidly evolve through the Hertzsprung gap as yellow giants and supergiants (YSG), before settling into the red giant branch. Identifying Hertzsprung gap stars in nearby galaxies is crucial for pinpointing progenitors of luminous red novae (LRNe) – astrophysical transients attributed to stellar mergers. In the era of extensive transient surveys like the Vera Rubin Observatory's Legacy Survey of Space and Time (LSST), this approach offers a new way to predict and select common envelope transients.

Aims. This study investigates potential progenitors and precursors of LRNe by analysing *Hubble Space Telescope* (HST) photometry of stellar populations in galaxies within ~ 20 Mpc to identify YSG candidates. Additionally, we use the Zwicky Transient Facility (ZTF) and MeerLICHT/BlackGEM to identify possible precursors, preparing for future observations by the LSST.

Methods. We compiled a sample of 369 galaxies with HST exposures in the $F475W$, $F555W$, $F606W$, and $F814W$ filters. We identified YSG candidates using MESA stellar evolution tracks and statistical analysis of colour-magnitude diagrams (CMDs).

Results. Our sample includes 246,573 YSG candidates with masses between $3M_{\odot}$ and $20M_{\odot}$ and is affected by various contaminants, notably foreground stars and extinguished main-sequence stars. After excluding foreground stars using *Gaia* proper motions, contamination is estimated at 1.7% from foreground stars (based on TRILEGAL simulations) and $\sim 20\%$ from extinction affecting main-sequence stars. Combining our YSG candidates with time-domain catalogues yielded several interesting candidates. In particular, we identified twelve LRN precursor candidates for which followup is encouraged.

Conclusions. We highlight the importance of monitoring future transients that match YSG candidates to avoid missing potential LRNe and other rare transients. LSST will be a game changer in the search for LRN progenitors and precursors, discovering over 300,000 new YSG candidates and 100 LRN precursors within 20 Mpc.

Key words. Hertzsprung–Russell and colour–magnitude diagrams – novae – catalogues – Vera Rubin

1. Introduction

The termination of hydrogen burning in a stellar core marks the end of a star's main sequence (MS) phase. As the core contracts and temperatures rise, hydrogen shell burning starts, causing the star to expand rapidly. This expansion leads to the star becoming progressively larger and cooler, transitioning into the yellow giant (YG) and supergiant (YSG) phase. However, this evolutionary stage is brief and difficult to observe, creating a "gap" between the MS and the Red Giant Branch (RGB) in the Hertzsprung-Russell (HR) diagram, known as the Hertzsprung gap. Early surveys of YSGs in the Milky Way, Magellanic Clouds, and Andromeda revealed significant discrepancies between observations and stellar evolution models, particularly in estimating the duration of this phase (Massey et al. 2000; Drout et al. 2009; Neugent et al. 2010; Drout et al. 2012).

Adding further complexity, most massive stars are found in binary or multiple systems, with 70% of O-type stars and 50% of B-type stars having companions (e.g., Moe & Di Stefano 2017 and references therein). The rapid expansion of YSGs in such systems often triggers interactions like Case B mass transfer and substantial mass loss (Marchant & Bodensteiner 2023). This interaction makes the YSG phase particularly valuable for studying binary evolution. In cases where a YSG is part of a binary system, unstable mass transfer can lead to a common envelope phase (Paczynski 1976). The transfer of angular momentum of the binary into the envelope can result in its partial (or total) ejection, producing a rare astrophysical transient known as a Luminous Red Nova (LRN). While YSGs have been linked to other rare transients, such as core-collapse supernovae (SNe) (Smart 2015) and failed SNe (Georgy 2012; Neustadt et al. 2021), they are most notably identified as progenitors of LRNe (MacLeod et al. 2017; Blagorodnova et al. 2017, 2021; Cai et al. 2022).

LRNe are optical and infrared transients with luminosities between those of novae and supernovae, evolving over several

[★] Tables 3 and 4 are only available in electronic form at the CDS via anonymous ftp to cdsarc.cds.unistra.fr (130.79.128.5) or via <https://cdsarc.cds.unistra.fr/cgi-bin/qcat?J/A+A/>

weeks to months. Their peak brightness correlates with the progenitor’s mass (Kochanek et al. 2014; Blagorodnova et al. 2021), enabling us to investigate binary evolution across a wide range of stellar masses, from low-mass to massive stars. Unlike optical LRNe, infrared LRNe may result from common envelope ejections in stars more evolved than YSGs (MacLeod et al. 2022). These stars experience significant mass loss, causing them to become obscured in optical wavelengths while remaining detectable in the infrared. The most well-studied LRN to date, V1309 Sco, was discovered in the Milky Way. Extensive photometric data up to seven years before the onset of the transient revealed its progenitor, a contact binary system with a quickly decaying period, possibly evolving to the merger of its components (Tylenda et al. 2011). Interestingly, the light curve of V1309 Sco exhibited a slow, steady brightening beginning approximately five years prior to the merger. Similar precursor emissions have been observed in extragalactic LRNe (Kankare et al. 2015; Blagorodnova et al. 2017, 2020; Pastorello et al. 2019, 2021a), though their greater distances and faintness have made it difficult to achieve equally detailed sampling. It remains an open question whether this precursor phase reflects continuous or episodic mass loss in the years leading up to the major outburst, potentially signaling the early stages of a binary system merger. Long-term observations of LRN progenitor stars are therefore crucial for testing their binary origins and gaining valuable insights into pre-merger mass loss episodes in these systems.

The primary challenge in detecting precursors is their modest absolute magnitude, which means most extragalactic LRNe are only identified during their brightest outbursts. The lack of deep archival data further complicates efforts to detect precursor brightening. To overcome this, a comprehensive catalog of potential progenitors in nearby galaxies is essential. A large and deep survey is mandatory to achieve such a goal. While early discoveries of LRNe were limited to the Milky Way and M31 (e.g., V4332 Sgr and V838 Mon, Martini et al. 1999; Tylenda & Soker 2006; M31 LRN-2015, Williams et al. 2015; Blagorodnova et al. 2020), the advent of large synoptic surveys, such as ATLAS (Tonry et al. 2018), the Zwicky Transient Facility (ZTF; Bellm et al. 2019), MeerLICHT (Bloemen et al. 2016), and BlackGEM (Groot et al. 2019, 2024), has paved the way for the systematic detection of LRNe throughout the Local Group and beyond (e.g. Karambelkar et al. 2023). The upcoming Vera C. Rubin Observatory, with its Legacy Survey of Space and Time (LSST), promises to revolutionize transient astronomy, providing an unprecedented opportunity to detect faint LRNe and LRN precursors across vast distances. With LSST expected to generate 10 million transient alerts daily, the primary challenge will be identifying LRN precursors amidst this vast data unless a targeted strategy is developed to detect them.

In this study, we present a strategy for identifying LRN precursors by cataloging YSG candidates within 20 Mpc, leveraging archival *Hubble Space Telescope* (HST) photometry. Our goal is to identify potential precursor candidates by cross-matching future transient alerts with this catalog, offering a new approach to studying the processes driving LRN precursor brightening and triggering mechanisms. An initial study provided a similar census of YGs and YSGs in the Milky Way (Addison et al. 2022). Using *Gaia* DR2 and EDR3 (Gaia Collaboration et al. 2018, 2021) sources, they modelled the distribution of a sample of Milky Way stars in the colour-magnitude (M_G vs. $BP - RP$) diagram. Statistical modelling allowed them to select the Hertzsprung gap as the least-populated region of the diagram. As a result, they identified 21 candidates exhibiting signs of a

steady increase in brightness. Most of these candidates showed Balmer lines in emission and an infrared excess in their spectral energy distributions, reinforcing the likelihood of an accreting system with dust production. Interestingly, one of them turned out to be the precursor of a type-I X-ray burst (Reig et al. 2022).

While the census of Galactic YSG candidates is crucial, the rate of LRNe is comparable to that of core-collapse supernovae (Karambelkar et al. 2023), suggesting that the largest population of LRN precursors may be found beyond our Galaxy. To address this, we apply a similar methodology to catalog extragalactic YSGs using archival HST photometry of galaxies within 20 Mpc. If a future transient alert matches an object in this catalog, it could be flagged as a potential precursor and prioritized for follow-up observations. This approach offers a practical strategy to sift through the vast number of LSST alerts and conduct the first in-depth study of the processes driving LRN precursor brightening.

The paper is structured as follows: in Section 2 we define the data and methods used to select the samples and remove contaminants. Section 3 presents a statistical description of the selected sample and the different sources of contamination. We crossmatched this catalogue to LRN progenitors from the literature, to the Transient Name Server¹ (TNS) and to time-domain surveys in Section 4, showcasing some individual precursor candidates. These results are discussed in Section 5 and compared to previous searches for YSGs and LRN progenitors. We conclude and give some guidance on how to use this catalogue in Section 6.

2. Methods

2.1. Selection criteria

To identify progenitors of transients produced by massive stars, we need a YSG sample complete down to $8 M_{\odot}$. This completeness is key for future population studies. According to MESA (Modules for Experiments in Stellar Astrophysics, Paxton et al. 2011) stellar models, an $8 M_{\odot}$ star crossing the Hertzsprung gap has an absolute magnitude of $M_{F814W} \sim -5$. HST can detect such a star up to 20 Mpc away with a 1-hour exposure ($m_{lim,F814W} \sim 27.5$). Shorter typical exposures (e.g., 600s) only detect YSGs down to $16 M_{\odot}$ at this distance. Thus, our sample is limited to galaxies within 20 Mpc with deep HST exposures in several bands, allowing us to conduct a census of stars in the Local Universe up to the Virgo cluster, and ensuring a minimum completeness limit of $16 M_{\odot}$ to cover the Hertzsprung gap.

To get a complete sample of nearby galaxies, we use the HECATE catalogue of galaxies (Heraklion Extragalactic CATALOGUE, Kovelakas et al. 2021), based on the HyperLEDA database (Paturel et al. 2003) but supplemented with robust distance estimates, galaxy mass, metallicity and star formation rate. The base sample, containing 1883 galaxies closer than 20 Mpc, is crossmatched with HST observations available on the *Mikulski Archive for Space Telescopes* (MAST), to find galaxies with overlapping deep ($t_{exp} > 300$ s) exposures in two optical filters². The list of selected filters is detailed in Table 1, together with the number of galaxies selected for each filter. We select the $F475W$, $F555W$, $F606W$ and $F814W$ filters because they have responses close to the Johnson-Cousins V ($F475W$, $F555W$, $F606W$) and I ($F814W$) filters, allowing us to study V against $V - I$ colour-

¹ <https://www.wis-tns.org/>

² This crossmatch was performed using the API of MAST, available as part of the astroquery v0.4.6 package (Ginsburg et al. 2019)

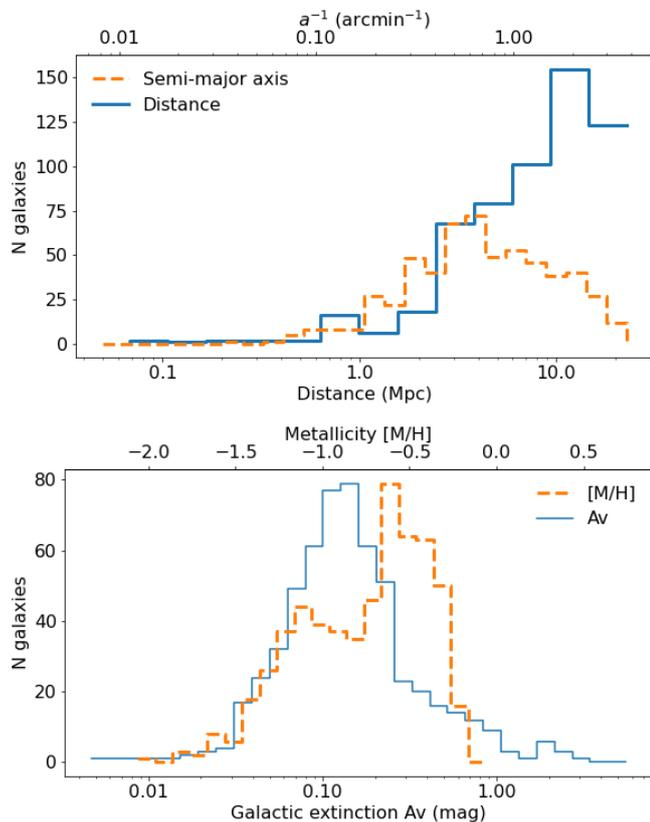


Fig. 1. Distribution of some properties of the sample of 575 HST-observed galaxies. (Top) Semi-major-axis a and distance from HECATE. (Bottom) Metallicity and Galactic extinction (see text for details).

magnitude diagrams (CMD). The resulting HST-observed sample contains 575 galaxies. The distributions of distance and angular sizes are shown in the top panel of Figure 1.

2.2. HST data retrieval

To retrieve HST sources, we use two databases comprising third-party catalogues in which source extraction has already been performed. The third release of the Hubble Source Catalog (HSCv3, Whitmore et al. 2016) includes *Advanced Camera for Surveys* (ACS) and *Wide-Field Camera 3* (WFC3) data that were public as of 2017 October 1. As such, it contains data for 449 of our galaxies observed before this date. HSCv3 data were retrieved using MAST queries with the CasJobs API³. For 118 additional galaxies, whose observation requirements are met only after 2017, we retrieve their source catalogues from MAST. At the time of the writing, eight galaxies could not be retrieved in these databases, due to proprietary exposures or missing source catalogues. As an example, the southern region of M31, which has sparse coverage in HSCv3, is included in the MAST retrieval. This leads to uniform coverage of the inner galaxy, as shown in Figure 2).

The MAST third party catalogues were produced at the time of the data reduction of the corresponding observations, using either DAOPHOT (Stetson 1987), SExtractor (Bertin & Arnouts 1996), or the Hubble Advanced Products pipeline (Tran et al. 2020). For both types of catalogues, magnitudes are retrieved in the large aperture photometry (*MagAper2*). We made sure

³ <https://github.com/rlwastro/mastcasjobs>

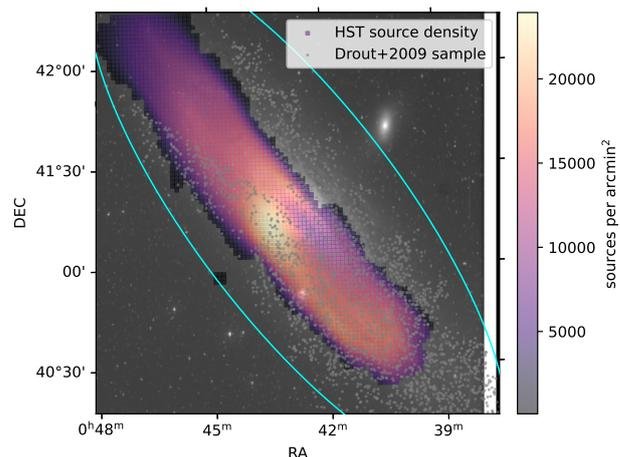


Fig. 2. Density of HST sources under study for the galaxy M 31, as retrieved through HSCv3 and MAST databases. The background image is from the Digitized Sky Survey 2 (DSS2, Lasker et al. 1996).

Instrument	Red filter	Green Filter	N galaxies
ACS	<i>F814W</i>	<i>F606W</i>	210
		<i>F555W</i>	40
		<i>F475W</i>	47
WFC3	<i>F814W</i>	<i>F606W</i>	14
		<i>F555W</i>	54
		<i>F475W</i>	23
WFPC2	<i>F814W</i>	<i>F606W</i>	116
		<i>F555W</i>	71

Table 1. HST filters used in this study. The last column gives the number of galaxies selected in the corresponding filters.

that MAST catalogues are reliable and have well calibrated photometry, by comparing their sky coverage and their CMD with HSCv3 data for two test galaxies (NGC 45 and ESO 209-9). In all tested filters, the bias and standard deviation between HSCv3 and MAST photometry is < 0.05 mag and < 0.2 mag, respectively. Once downloaded, all catalogues of a given galaxy are merged and crossmatched to obtain a single “master” catalogue, using *astropy* v5.3.3 (Astropy Collaboration et al. 2013)⁴. To discard compact star clusters and cosmic rays, we discarded sources with concentration indexes (CI) < 0.85 or magnitude errors > 0.1 .

2.3. CMD analysis

2.3.1. Stellar evolution tracks

To analyse the CMD of galaxies, a physical reference is needed, such as isochrones or stellar evolution tracks in the observer’s frame. However, the shape of an observed CMD heavily depends on intrinsic and extrinsic parameters. Intrinsic parameters include the galaxy star formation history and its metallicity, while extrinsic parameters correspond to measurement uncertainties and the extinction along the line of sight, commonly modelled with the extinction parameter A_{λ} . Using the synthetic photometry of stellar evolution tracks provided by MIST (MESA

⁴ A data-dependent matching radius r_1 ($0.3 < \frac{r_1}{\text{arcsec}} < 2$) is used to associate sources from different filters, and another one r_2 ($0.1 < \frac{r_2}{\text{arcsec}} < 0.3$) is used to eliminate duplicate sources.

Parameter	Values
ZAMS mass M_*/M_\odot	{3, 4, 6, 8, 10, 12, 14, 16, 18, 20}
Metallicity Z	{-1.2, -0.9, -0.6, -0.3, 0}
Extinction A_V	{0, 0.2, 0.4, 0.6, 0.8, 1, 1.5, 2}

Table 2. MIST grid of parameters.

Isochrones & Stellar Tracks⁵, Dotter 2016; Choi et al. 2016), we generated tracks for a grid of zero-age main sequence (ZAMS) stellar masses, extinctions, and metallicities, summarised in Table 2. The ranges of extinctions and metallicities correspond to the ranges of estimated Galactic extinctions and metallicities of galaxies in our sample, and the mass range encompasses most of known LRNe progenitors (e.g. MacLeod et al. 2022). The upper limit of the mass range does not restrict the YSG selection; instead, it marks the point beyond which stellar masses become poorly estimated, as the Hertzsprung gap can no longer be consistently defined as a continuous post-MS phase.

To estimate extinctions along the line-of-sight for each HECATE galaxy, we use the 2D dust map of Delchambre et al. (2023) released as part of *Gaia* DR3. Metallicities and galaxy masses are provided in HECATE for only 15% (276) and 62% (1159) of our base sample, respectively. To estimate metallicities, we therefore relied on the absolute B magnitude – oxygen abundance relations of Pilyugin et al. (2004) (Equations 12 and 15 for spiral and irregular galaxies, respectively⁶): $12 + [O/H] = \min(5.8 - 0.139 B_{\text{abs}}, 6.93 - 0.079 B_{\text{abs}})$. Gas-phase oxygen abundances were converted to metallicity using the relation $Z = [M/H] = 12 + [O/H] - 8.69$, where 8.69 is the solar oxygen abundance given in Asplund et al. (2009). The resulting distributions of Galactic extinction and metallicity are shown in Figure 1 (bottom panel). In the following, all CMDs are in the Vega magnitude system, aperture-corrected (using the table⁷ recommended by the HSCv3 documentation) and de-reddened of Galactic extinction.

2.3.2. HR gap definition

The Hertzsprung gap of each galaxy is identified using the MIST tracks at different masses. Specifically, we define this gap as the time interval between two points, the post-MS bright turnoff (the point when the V -band luminosity first reaches 95% of its post-MS bright turnoff value), and the pre-RGB faint turnoff, as illustrated in Figure 3 by the left-hand and right-hand solid blue lines. To account for the internal extinction of the galaxy and retrieve extinguished YSG candidates, we artificially applied a 0.4 mag extinction to the red-side selection cut, using a relative visibility value of $R(V) = 3.1$. Although this additional extinction is arbitrary, it ensures the retrieval of most extinguished candidates, as discussed in Section 2.4. YSG candidates are searched between these lines and above the MIST track of a reference ZAMS star mass, which ranges from 3 to 16 M_\odot depending on the galaxy. To ensure the completeness of the selected samples at this reference mass, it is chosen to be the smallest mass for which the faint end of the Hertzsprung gap is well-observed, i.e., significantly brighter than the sensitivity of HST exposures. Consequently, we exclude 102 galaxies where the available HST data

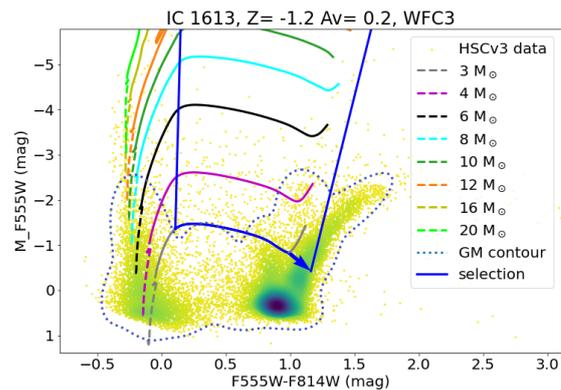


Fig. 3. An example of CMD analysis. Extinction-corrected CMD of IC 1613 sources with MIST tracks for a metallicity $Z=-1.2$ and an extinction of $A_V=0.2$. Hertzsprung gap candidates are selected above blue lines. The dotted contour shows the Gaussian mixture model representing the data.

are too shallow to accurately detect YSGs with masses of 16 M_\odot or below.

2.3.3. Statistical modelling

Due to the significant uncertainties in the estimate of distance, metallicity, Galactic extinction, HST photometry of faint sources, and stellar evolution models, a mismatch between the true locus of the observed Hertzsprung gap and its MIST estimate is inevitable for some galaxies. In particular, some galaxies have part of their MS and/or RGB intersecting the selected area of the CMD. To exclude these densely populated regions, we adopt a similar approach as the YSG selection method of Addison et al. (2022). The CMD of each galaxy is statistically modelled as a mixture of gaussian components (Gaussian Mixture, GM). The number of components is determined based on the logarithm of the number of sources, balancing the need to avoid overfitting in sparse CMDs while allowing for the fitting of complex structures in dense CMDs. To better retrieve the tails of the distribution (i.e. CMD features such as the RGB), the faintest and most populated regions of dense CMDs, as estimated by Kernel Density Estimation (KDE), were artificially depopulated by a factor of up to 20. This step only removes sources in faint regions and not the YSG selection area.

To exclude the dense regions of the CMD, sources located within the GM contour of a reference likelihood are discarded. This contour intersects the Hertzsprung gap of the reference MIST track, with the likelihood value optimised through visual inspection. The resulting contour for IC 1613 is shown by the dotted line in Figure 3, where the reference MIST track corresponds to a 3 M_\odot star. The red giant branch is well excluded from the YSG selection area. A representative subset of the CMDs analysed in this study is shown in Appendix A. This statistical modelling requires a minimum of 100 sources to provide a reliable CMD match. Therefore, we discarded 96 galaxies, leaving 369 galaxies in our sample.

⁵ <https://waps.cfa.harvard.edu/MIST>

⁶ Given that only 12 galaxies in our sample are elliptical, we apply this relation accordingly

⁷ https://archive.stsci.edu/hst/hsc/help/HSC_Faq/ci_ap_cor_table_2016.txt

2.4. Sample cleaning

2.4.1. Removing known contaminants

Different types of contaminants may be included at this stage of the selection. First, the line of sight chance alignment of Milky Way stars, notably yellow dwarfs and white dwarfs, with the galaxy under consideration can cause them to appear within the Hertzprung gap of its CMD. Likewise, background objects such as quasars can also appear in this locus. Second, the extinction affecting main-sequence stars inside each galaxy can displace them from the MS to the Hertzprung gap in the observed CMD. Additionally, objects other than YSG also naturally appear in the Hertzprung gap, such as cepheids and other variables within the instability strip, luminous blue variables (LBV), or unresolved globular clusters (e.g. Kraft 1966; Justham et al. 2014; Mora et al. 2007).

As an initial cleaning process, we crossmatched between our sample and the *Simbad*⁸ and *Gaia DR3* (Gaia Collaboration et al. 2023b) catalogues using a matching radius of 0.5". *Simbad* quasars, globular clusters, and classical cepheids were discarded. Additional quasars were found and excluded using the *Milliquas* (Flesch 2021) and *Gaia* Extragalactic (Gaia Collaboration et al. 2023a) catalogues. However, we flagged known LBVs and yellow/red supergiants for further consideration within the sample. Sources exhibiting significant *Gaia* proper motion ($PM/PM_{\text{err}} > 4$) are identified as Galactic and discarded. Although other types of contaminants cannot be directly excluded, their presence can be quantified statistically.

2.4.2. Quantifying foreground contamination

To estimate the line of sight foreground contamination towards each galaxy, we utilised the TRILEGAL (TRIdimensional model of the GALaxy, Girardi et al. 2005) simulation, which models the Milky Way's stellar content, incorporating the Sun's position and various Galactic components. It includes the thin disc, thick disc, halo, and bulge, along with their star formation histories. This simulation, notably used by Dal Tio et al. (2022) to simulate the Milky Way as observed by the upcoming LSST survey, and accessible through an API from NOIRLab⁹, simulates the photometry and stellar parameters of the observed Galactic population along designated lines of sight. Patches of 0.25 deg² were queried for each galaxy in our sample. Given that LSST's coverage is mostly restricted to the Southern Hemisphere ($\text{Dec} < 0$), some galaxies lie outside the simulated regions. For cases where LSST covers the symmetric position relative to the Sun-Galactic poles plane, we used this position instead, assuming similar results due to the symmetric nature of TRILEGAL components. This planar symmetry was verified using test coordinates through the TRILEGAL web interface¹⁰. For the 30% of galaxies (106 in total) still uncovered, we utilised the TRILEGAL web interface with the same parameters as Dal Tio et al. (2022). Notably, the halo profile in the web interface differs from the LSST simulation, employing a $r^{-1/4}$ profile versus Dal Tio et al.'s $r^{-1/2.5}$ profile. We adjusted for this by approximating the profile with $r^{-1/4}$, $\Omega = 0.0025 M_{\odot} \text{pc}^{-3}$ and $r_h = 5700 \text{pc}$, based on comparable star counts and magnitude distributions.

TRILEGAL sources matching the footprint of the selected HST exposures and exhibiting synthetic HST photometry within the specific Hertzprung gap selection region are identified as

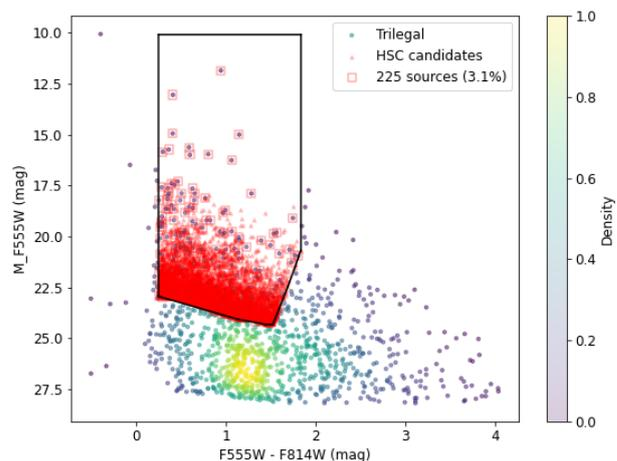


Fig. 4. Illustration of the estimation of foreground contamination rate using the TRILEGAL Milky Way simulations. The CMD shows TRILEGAL sources overlapping with the footprint of M83 HSC sources. Highlighted in red are the YSG candidates identified within this sample. TRILEGAL sources falling within the black polygon, circled in red, are identified as foreground contaminants. They represent 3.1% of the M83 YSG candidates.

contaminants. Figure 4 illustrates this method for M83, showing the CMD of TRILEGAL sources overlapping with HST exposures and overlaying the observed YSG candidates. The results of this foreground contamination analysis are presented in Section 3.2.

2.4.3. Extinguished main-sequence stars

Although we account for the Galactic extinction along the line of sight for each galaxy using the appropriate MIST model, intrinsic extinction inside each galaxy is not modelled at this stage. Consequently, a significant fraction of Hertzprung gap sources may actually be extinguished MS stars. To quantify this, we assigned to each candidate a probability to be an extinguished main-sequence star. Assuming a normal distribution for extinction, we measured extinction scatter by evaluating the standard deviation of A_V in a thin region of the CMD, chosen to be the red giant branch, as illustrated in Figure 5. This standard deviation is used to model the additional extinction in the selection region, resulting in a probability map for each CMD (Figure 5, bottom panel). This probability is naturally highest at the blue edge of the selection region, which separates the main-sequence region from the Hertzprung gap. By averaging these probabilities on a per-galaxy basis, we can determine the contamination rate due to extinction. The distribution of A_V scatters estimated for all selected galaxies is shown in Figure 6. Besides providing contamination probabilities, it also suggests that the 0.4 mag extinction applied to the red edge of the selection region is sufficient to recover most of the extinguished YSG (Section 2.3.2).

3. Results

3.1. Selected candidates

Our analysis identified a total of 246,573 YSG candidates, a portion of which being listed in Table 3. The cumulative distribution of their distances is depicted in Figure 7, indicating that about 25% of these candidates are located in galaxies at approximately 0.8 Mpc. These candidates are actually located in M 31 (53,323

⁸ <https://simbad.cds.unistra.fr/>

⁹ https://datalab.noirlab.edu/lsst_sim/index.php

¹⁰ Available at <http://stev.oapd.inaf.it/cgi-bin/trilegal>

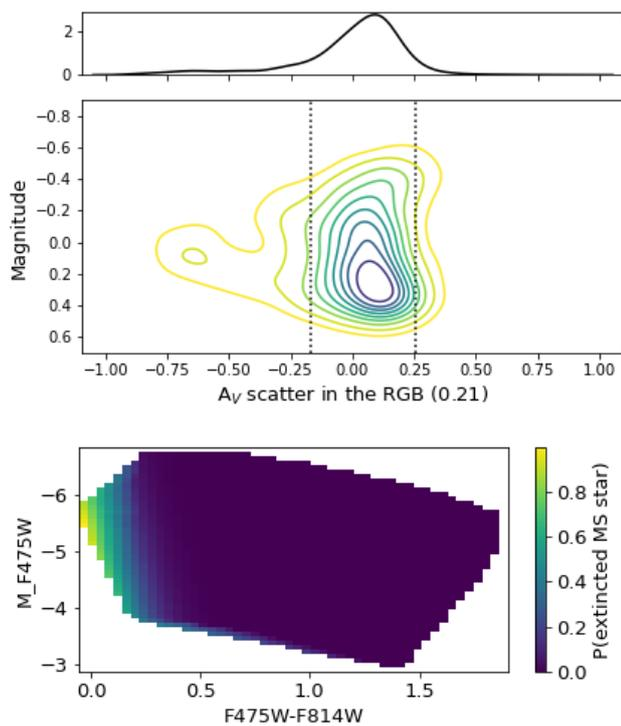


Fig. 5. (Top) Density plot of the RGB of IC 1613 in the (Magnitude - A_V) plane. The top curve shows the KDE of A_V values, with a standard deviation of ± 0.21 (dotted lines). (Bottom) Resulting probability map to be an extinguished MS star in the selection region of YSG sources in the IC 1613 galaxy.

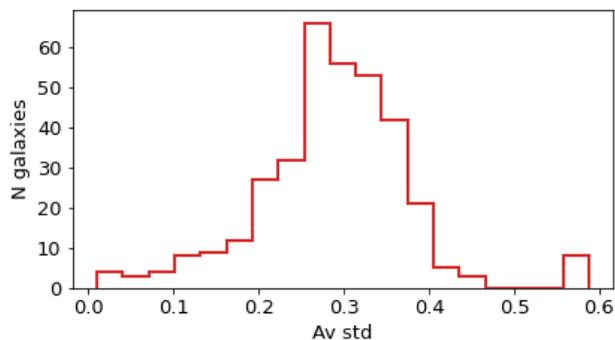


Fig. 6. Distribution of the standard deviations of extinction for our galaxy sample.

candidates) and M 33 (15,706), the two galaxies with most candidates. The three next galaxies with the most YSG candidates are M101 (15,156), NGC 300 (9,706), and NGC 253 (8,004).

As a result of the CMD analysis, we identified YSG candidates in 355 galaxies. The HST data provenance, available blue/green filter, coverage, and the parameters used for fitting the CMD as described in Section 2.3 are provided for each galaxy in Table 4. This table also details the number of candidates for each galaxy and the estimated contribution from different contaminants.

YSG candidates exhibit apparent magnitudes in the $F814W$ band ranging from 16 to 25, with a peak at approximately 22.2 (Figure 8). Single-star ZAMS stellar masses, luminosities, and temperatures for these candidates were estimated by interpolation using the MIST stellar evolutionary tracks within the

ID	Galaxy	ra (deg)	dec (deg)	m_{F814W} (mag)	M_* (M_\odot)	$\log(T_{\text{eff}} \text{ (K)})$	P_{extin}
1	Dra dSph	260.47560	57.95323	16.8	3.8	3.75	0.07
2	Dra dSph	260.10617	57.97408	15.6	6.0	3.73	0.00
3	Dra dSph	260.10771	57.97393	16.3	4.3	3.79	0.17
4	Dra dSph	260.07129	57.97381	15.9	5.4	3.75	0.01
5	Dra dSph	260.09113	57.97427	16.9	3.8	3.84	0.42
6	Dra dSph	260.20050	57.91569	17.6	3.2	3.74	0.02
7	Dra dSph	260.10907	57.97411	15.5	5.9	3.73	0.01
8	Dra dSph	260.07055	57.97380	15.7	5.7	3.74	0.00
9	Dra dSph	260.06858	57.97374	15.8	5.6	3.72	0.00
10	Dra dSph	260.09112	57.97362	17.0	3.6	3.78	0.13
11	Dra dSph	260.10544	57.97412	15.7	5.6	3.74	0.01
12	ESO 104-22	283.90293	-64.80823	22.2	15.7	3.63	0.00
13	ESO 104-22	283.92116	-64.80982	23.2	11.2	3.85	0.75
14	ESO 104-22	283.91606	-64.80495	21.9	15.7	3.67	0.02
15	ESO 104-22	283.91053	-64.80493	24.0	8.8	3.69	0.04
16	ESO 104-22	283.93422	-64.81086	22.6	13.9	3.64	0.00
17	ESO 104-22	283.93325	-64.80926	22.7	12.2	3.73	0.12
18	ESO 104-22	283.90344	-64.80865	22.4	14.0	3.79	0.37
19	ESO 104-22	283.93478	-64.81320	24.0	8.7	3.69	0.04
20	ESO 104-22	283.92837	-64.81673	24.0	8.8	3.69	0.04
21	ESO 104-22	283.90688	-64.81096	22.4	13.5	3.77	0.27
22	ESO 104-22	283.92554	-64.81018	24.1	9.0	3.82	0.51
23	ESO 104-44	287.85375	-64.22362	24.3	8.9	3.67	0.01
24	ESO 104-44	287.85099	-64.22005	23.7	10.8	3.65	0.00
25	ESO 104-44	287.85434	-64.22405	24.2	8.8	3.82	0.44
26	ESO 104-44	287.85947	-64.22657	24.4	8.8	3.90	0.97
27	ESO 104-44	287.85444	-64.21808	21.9	15.4	3.75	0.12
28	ESO 104-44	287.85261	-64.22444	23.8	10.2	3.65	0.00
29	ESO 104-44	287.85741	-64.21309	22.2	14.2	3.63	0.00

Table 3. List of YSG candidates. Column 2: host galaxy. Columns 3–5: HST coordinates (deg) and magnitude (mag). Columns 6–7: MIST inferred stellar parameters. Column 8: Probability to be an extinguished MS star. The complete list will be made available in electronic form.

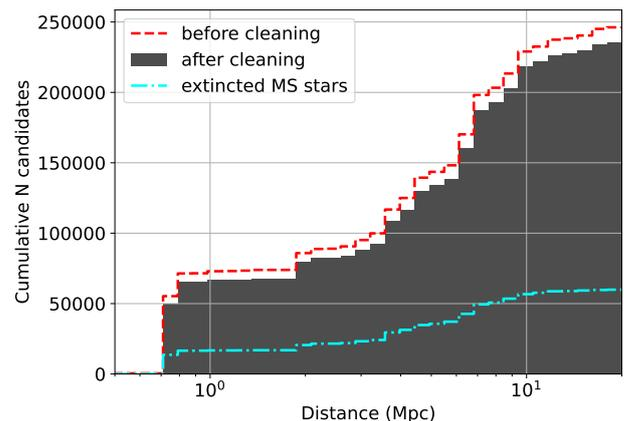


Fig. 7. Cumulative distribution of distances for YSG candidates before and after cleaning, and estimated number of extinguished main-sequence stars.

Hertzsprung gap. The distribution of stellar masses, shown in Figure 8, appears bimodal: a lower-mass peak, around approximately $5M_\odot$, primarily corresponds to candidates in M31, M33 and NGC 253, and a higher-mass peak, around approximately $10M_\odot$, corresponds to more distant candidates. This bimodality is further illustrated in Figure 9, showing the tight correlation between interpolated stellar masses and $F814W$ absolute magnitude.

3.2. Contamination fraction

To evaluate the contamination fraction from intrinsic extinction and foreground sources, we considered various types of contaminants. Foreground contamination was quantified using the TRI-LEGAL star counts. According to the method detailed in Sec-

Galaxy	Distance (Mpc)	HSTcov (%)	Source	Camera / Filter	N _{src}	MIST M _{*,ref} (M _⊙)	A _V (mag)	[Fe/H]	n _{GM}	N _{cand}	f _{extin}	f _{foreground}
M 31	0.8	34.3	HSCv3+MAST	ACS F475W	97929	4	0.49	-0.88	0	53323	0.251	0.136
M 33	0.8	10.0	HSCv3	ACS F475W	2834135	4	0.51	-1.13	10	15706	0.183	0.137
Sgr dIG	1.1	100.0	HSCv3	ACS F606W	13513	3	0.20	-1.47	50	357	0.306	0.446
Sex A	1.4	72.9	HSCv3	WFPC2 F555W	5710	4	0.16	-1.19	20	499	0.185	0.028
NGC 55	2.2	10.7	HSCv3	ACS F606W	146004	6	0.13	-1.45	10	2630	0.352	0.003
NGC 7793	3.4	57.0	HSCv3	ACS F555W	90987	8	0.06	-0.57	50	946	0.226	0.029
NGC 5253	3.5	100.0	HSCv3	ACS F555W	62144	8	0.11	-1.02	50	801	0.239	0.046
NGC 247	3.8	35.5	HSCv3	ACS F606W	277045	8	0.03	-0.55	20	512	0.294	0.045
NGC 253	3.9	41.5	HSCv3	ACS F606W	634859	8	0.37	-0.93	10	8004	0.353	0.005
ESO 223-9	4.4	100.0	HSCv3	ACS F606W	15109	8	0.60	-1.05	90	486	0.267	0.516
ESO 137-18	4.7	96.7	HSCv3	ACS F606W	19885	8	0.54	-0.83	30	578	0.193	0.437
M 83	4.8	37.7	HSCv3	ACS F555W	201354	8	0.16	-0.83	10	7158	0.287	0.031
NGC 45	5.8	82.3	HSCv3	ACS F555W	13503	8	0.19	-0.61	50	470	0.190	0.035
IC 5052	5.9	75.8	HSCv3	ACS F606W	39959	8	0.17	-0.98	50	929	0.332	0.042
IC 1959	6.4	100.0	HSCv3	ACS F606W	12641	8	0.09	-0.86	50	302	0.333	0.007
NGC 1566	6.5	47.3	HSCv3	ACS F555W	21651	8	-0.01	-0.63	20	2762	0.221	0.012
Fourcade-Figueroa	6.7	48.1	HSCv3	ACS F606W	38012	8	0.13	-1.26	0	593	0.288	0.136
NGC 3621	7.2	45.1	HSCv3	ACS F555W	67001	8	0.17	-1.01	0	6950	0.288	0.012
M 74	7.3	53.1	HSCv3	ACS F555W	59479	8	0.38	-0.86	20	6548	0.229	0.007
IC 4710	7.4	99.9	HSCv3	ACS F606W	26877	8	0.18	-0.73	20	920	0.280	0.126
UGC 3755	7.4	100.0	HSCv3	ACS F606W	4554	8	0.35	-1.03	50	301	0.236	0.021
NGC 2188	8.0	93.4	HSCv3	ACS F606W	16356	8	0.20	-0.63	50	1821	0.271	0.010
NGC 1433	8.3	58.9	HSCv3	WFC3 F555W	2308	10	0.14	-0.47	50	329	0.201	0.046
IC 4870	8.5	100.0	HSCv3	ACS F606W	4163	8	0.38	-0.97	80	532	0.186	0.015
NGC 7090	8.6	60.4	HSCv3	ACS F606W	14292	10	0.51	-1.12	50	1091	0.375	0.014
NGC 24	9.1	93.1	HSCv3	ACS F606W	18596	8	0.18	-1.26	0	881	0.366	0.009
NGC 4517	9.7	20.2	HSCv3	ACS F606W	3632	8	0.07	-0.50	70	314	0.155	0.023
ESO 373-8	9.8	71.9	HSCv3	ACS F606W	5719	10	0.51	-0.97	0	377	0.302	0.102
M 95	10.0	41.0	HSCv3	WFC3 F555W	3101	10	0.12	-0.98	0	405	0.211	0.015
IC 5201	10.3	72.8	HSCv3	ACS F606W	22810	10	0.14	-0.48	50	729	0.231	0.045
M 66	10.4	36.7	HSCv3	WFC3 F555W	29236	12	0.15	-0.56	0	2423	0.137	0.004
NGC 4592	11.2	98.5	HSCv3	WFC3 F555W	9412	10	-0.01	-0.88	10	828	0.208	0.007
NGC 5398	11.4	99.8	HSCv3	ACS F606W	14604	8	0.33	-1.11	0	1342	0.391	0.028
NGC 3810	16.2	94.4	HSCv3	ACS F555W	7386	16	0.40	-0.93	50	394	0.182	0.005

Table 4. List of galaxies having more than 100 YSG candidates, sorted by distance. Column 2: distance to the galaxy. Columns 3–6: information on their HST dataset. Columns 7–10: parameters used to fit their CMD. Column 11: number of resulting candidates. Columns 12–13: contamination estimates. The complete list of galaxies having YSG candidate will be made available in electronic form.

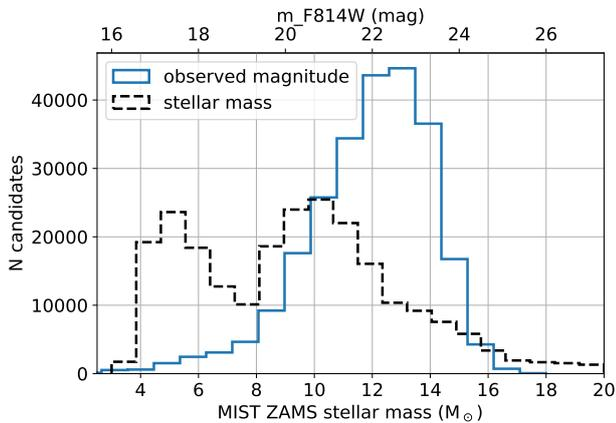


Fig. 8. Distributions of observed $F814W$ magnitude and stellar masses of YSG candidates.

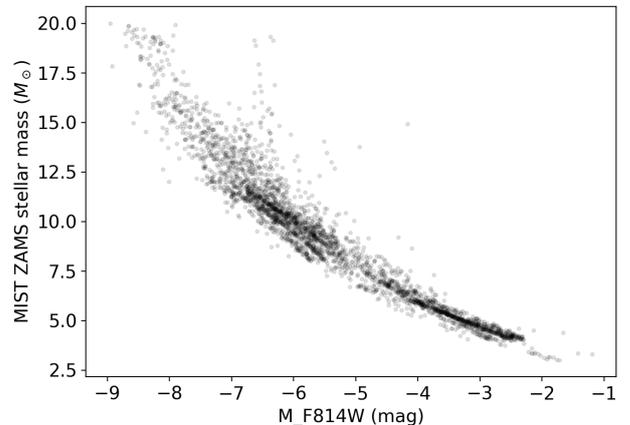


Fig. 9. MIST inferred ZAMS stellar masses of YSG candidates as a function of their absolute $F814W$ magnitude.

tion 2.4, approximately 5% of the sources in our YSG sample are expected to be foreground contaminants (including sources having high *Gaia* proper motion). The foreground contamination mainly affects galaxies at low Galactic latitudes ($|b| < 25^\circ$) and 75% of the galaxies have less than 10% of their YSG candidates being foreground, as shown in Figure 10 (right panel). As illustrated in this Figure, galaxies closer to the Galactic plane or toward the Galactic center exhibit higher contamination fractions. After using *Gaia* proper motions to clean the sample, removing 8,375 sources (3.4% of the sample), we therefore estimate the remaining foreground contamination to be $\sim 1.7\%$.

Additionally, the probability of each YSG candidate to be an extinguished main-sequence star was computed using the mod-

elled intrinsic extinction (Section 2.4). The mean probability for all sources in our YSG catalogue is 0.25, with the fraction of contaminants remaining constant across all distances (Figure 7). As expected, this probability is significantly influenced by the temperature of the source, and the filter used in the CMD analysis, as depicted in Figure 11.

Finally, contaminants such as quasars, Cepheids and luminous blue variables were identified and removed using *Gaia* and Simbad databases. These known contaminants represent a minority of the sample across all distances (Figure 7). These sources are typically brighter in both observed and absolute magnitudes, as shown in Figure 12. The clean sample of YSG contains 233,336 sources.

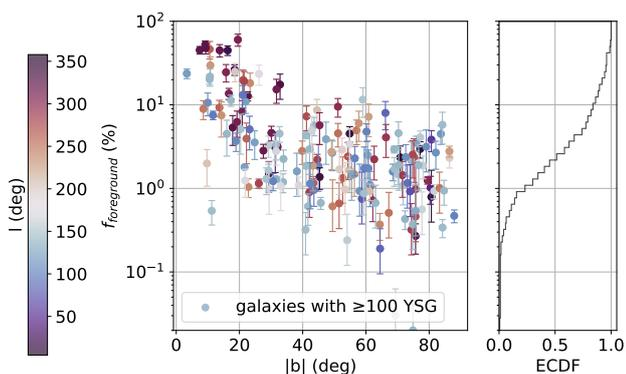


Fig. 10. (Left) Foreground contamination rate as a function of Galactic latitude, using the TRILEGAL Milky Way simulations. The colour encodes the Galactic longitude. To maintain readability, only galaxies with a minimum of 100 YSG candidates are included. (Right) Empirical cumulative distribution function (ECDF) of the foreground contamination rate. 75% of galaxies have less than 10% of their YSG candidates being foreground contaminants.

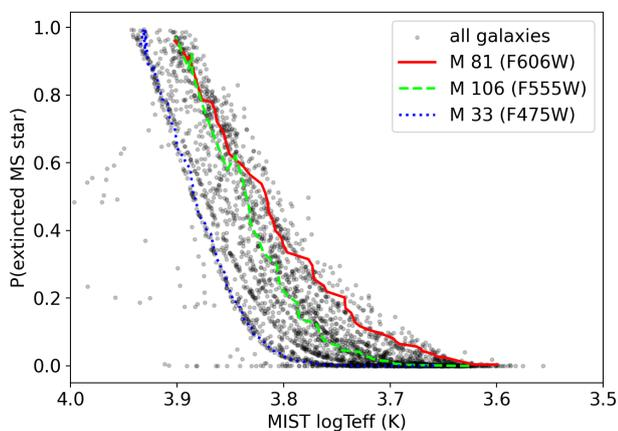


Fig. 11. Probability of YSG candidates to be an extinguished MS star as a function of their MIST temperature. Three example galaxies are shown, illustrating the impact of the HST blue/green filter used to analyse the CMD.

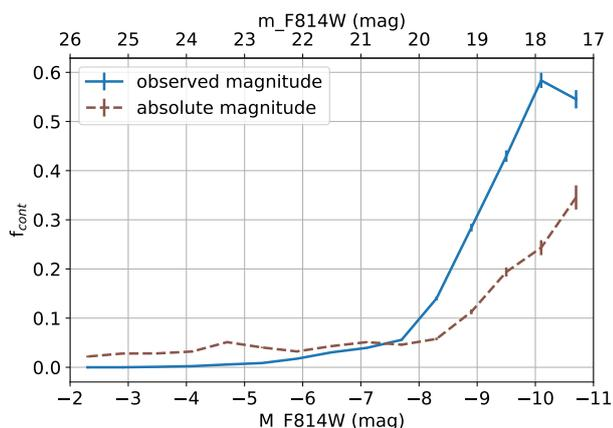


Fig. 12. Fraction of identified contaminants using Simbad and *Gaia* catalogues, as a function of observed and absolute $F814W$ magnitude.

LRN name	Distance (Mpc)	Status	Ref.
M31LRN2015	0.77	retrieved	[1]
AT2019zhd	0.78	not catalogued	[2]
AT2020hat	5.16	retrieved	[3]
M101-2015OT	6.4	outside HST	[4]
AT2018bwo	6.8	retrieved	[5]
AT2021biy	7.46	retrieved	[6]
AT2021blu	8.64	retrieved	[7]
NGC4490-OT	9.6	not catalogued	[8]

Table 5. LRN progenitors identified in the literature, and their retrieval status in our YSG sample. References: [1] MacLeod et al. 2017, [2] Pastorello et al. 2021a, [3] Pastorello et al. 2021b, [4] Blagorodnova et al. 2017, [5] Blagorodnova et al. 2021, [6] Cai et al. 2022 [7] Pastorello et al. 2023, [8] Smith et al. 2016a.

4. Applications

4.1. Completeness for known LRN progenitors

Many extragalactic LRNe discovered during the last decade had pre-outburst images taken several years before the transient (e.g. MacLeod et al. 2022 and references therein). For eight of them, listed in Table 5, their host galaxy is in our sample, allowing us to assess the rate of retrieved progenitors in our sample of YSG candidates. Three out of eight progenitors are missing in our sample. For AT2015dl, the transient is located outside the footprint of the HST observations. For NGC4490-OT, although the progenitor was measured and studied by Smith et al. (2016b), its apparent magnitude of $m_{F606W} = 23.58 \pm 0.24$ was too faint to be retrieved as an HSCv3 source (the faintest retrieved sources in a 30 arcsec radius circle around the progenitor position were 23.2 mag). For AT2019zhd, the progenitor had a low luminosity ($M_{F555W} = 0.21 \pm 0.14$, Pastorello et al. 2021a), placing it in the most populated region of the Hertzsprung gap. Consequently, it could not be selected after the Gaussian mixture cut. Moreover, its proximity to the edge of the field of view prevents this source from being retrieved as a MAST-catalogued source. Considering these results, our sample appears to represent a relatively comprehensive selection of LRN progenitors, with a $\sim 70\%$ completeness level in regions covered by HST.

4.2. Progenitors of past and ongoing transients: crossmatch to TNS

Our YSG sample can be used to find possible progenitors for past transients and further analyse them. To this end, we cross-matched our YSG candidates to the TNS public objects as of 2024 August 31st, with a match radius of 0.6". The resulting list of 32 transients is detailed in Table 6. About half of these transients are already classified and some are well-studied in the literature (e.g. SN2016bau: Aryan et al. 2021. SN2017ein: Van Dyk et al. 2018; Teffs et al. 2021. SN2024ggi: Pessi et al. 2024; Jacobson-Galán et al. 2024). For those, our HST matches may provide useful pre-outburst luminosity levels. The TNS report of AT2019ejn mentions multiple discoveries of this transient, suggesting it may be an LBV. For three other transients (AT2020aaqy, AT2021tmm and AT2021ytf), the $F814W$ magnitude is brighter than the TNS discovery magnitude, making them likely to also be variable stars. For twelve other transients, the type was not straightforwardly identified in TNS and they deserve a detailed analysis of their light curves and HST progenitors. Therefore, we inspected HST colour images for every candidate, using the Hubble Legacy Archive (HLA) website¹¹.

¹¹ <https://hla.stsci.edu/hlaview.html>

Galaxy	m_{F814W} (mag)	TNS name	Sep. (arcsec)	TNS Filter	m_{TNS} (mag)	M_{TNS} (mag)	type
NGC 3631	18.8	2016bau	0.08	Clear	17.8	-13.5	SN Ib
NGC 2403	20.2	2016ccd	0.16	Clear	18.0	-9.5	LBV?
M 31	19.8	2016ept	0.38	Clear	18.7	-5.7	–
M 31	21.3	2016fbx	0.26	Clear	17.7	-6.7	Nova
NGC 3938	24.2	2017ein	0.56	Clear	17.6	-13.5	SN Ic
NGC 45	22.6	2018bwo	0.13	Clear	16.4	-12.4	LRN
NGC 4449	21.7	2018mmb	0.55	r	19.7	-8.4	–
M 31	19.4	2019aacr	0.52	r	20.9	-3.6	V*
NGC 4449	20.0	2019ejn	0.41	Clear	18.8	-9.4	–
M 74	23.3	2019krl	0.01	g	21.0	-8.3	–
M 31	20.0	2020aaqy	0.35	r	20.9	-3.5	–
NGC 300	23.7	2020acll	0.59	Clear	18.4	-8.0	Nova
M 31	18.7	2020adbp	0.14	r	20.4	-4.1	–
NGC 5068	24.3	2020hat	0.02	orange	17.8	-10.7	LRN
NGC 1156	22.4	2020uq	0.28	Clear	17.1	-12.4	f.a.
NGC 1569	19.5	2021acz	0.28	Clear	14.0	-12.5	f.a.
NGC 6503	21.6	2021ahsv	0.17	r	20.1	-8.8	–
NGC 4631	21.4	2021biy	0.13	orange	18.1	-11.3	LRN
NGC 4228	21.6	2021blt	0.60	orange	18.5	-8.8	–
Spider	21.3	2021blu	0.12	orange	18.5	-11.0	LRN
M 31	18.0	2021lzk	0.24	r	19.3	-5.2	V*
NGC 5474	22.6	2021mjv	0.21	g	20.5	-8.8	–
M 31	19.8	2021tmm	0.28	r	20.5	-4.0	–
M 31	19.6	2021ytf	0.10	r	20.5	-4.0	–
NGC 253	19.5	2022llt	0.06	G	19.0	-9.0	–
NGC 3810	22.1	2022zut	0.22	orange	14.6	-16.5	SN Ia
M 101	23.2	2023azz	0.51	g	20.4	-8.7	–
M 31	21.7	2023wck	0.52	V	21.2	-3.2	microlensing?
NGC 3310	19.4	2023wgz	0.57	Clear	14.2	-17.1	–
M 31	21.8	2023wot	0.58	V	20.4	-4.0	–
NGC 3621	22.4	2024ggi	0.36	orange	18.9	-10.4	SN II
M 101	21.0	2024ikg	0.30	g	20.5	-8.6	–

Table 6. YSG candidates matching TNS objects. The last column shows the type according to TNS with eventual corrections (V*: variable star, f.a.: false alarm). Objects are sorted by TNS name.

Cutouts of 10 arcsec side-to-side are displayed in Figure 13 and the position of the transient is marked by a circle.

To inspect the temporal evolution of the candidates, we obtained forced photometry for the ZTF public data using the online service ZTF Forced Photometry Service (ZFPS) (Masci et al. 2023). For every candidate, we retrieved all the data starting from the beginning of the public survey in March 2018 (around MJD 58178). We generally used the difference imaging flux obtained during the first year of operations (or a period with low residual flux) as a baseline to calibrate the difference imaging magnitudes. We applied the quality cuts recommended in the documentation and we imposed `forcediffimchiSq` (Reduced chi-square in PSF-fit) < 1.3 . Data points with $S/N > 3$ were considered as detections and the upper limits are reported with a 5σ threshold. To increase the S/N for these faint objects, we binned the fluxes using a 15-day bin size. The resulting light curves are shown in Figure 14. In the following, we report the results of a detailed analysis aimed at identifying potential LRN precursors.

AT2016ept: this source matches a YSG in M31 MAST catalogues, with $m_{F814W} = 19.8$, $A_{F475W} = 21.9$. After inspection of the HLA image we found that this source is the confusion of several fainter sources ($m_{F814W} > 20.4$) that are well listed in HSCv3, although none of them is a YSG. The dips in its light curve could indicate the presence of an eclipsing binary system within this stellar environment, but there is no evidence of LRN precursor emission.

AT2018mmb: this transient is located at $0.55''$ from a faint ($m_{F555W} = 22.78$, $m_{F814W} = 21.68$) YSG in our sample, inside a stellar cluster. However, it is in a crowded region, surrounded by many sources that may cause source confusion ($CI = 1.4$), and a significantly brighter source ($m_{F555W} = 19.07$, $m_{F814W} = 19.38$) is located at just $0.37''$ from the transient. The position of this bright source in the CMD is close the locus of the MS. Although this neighbour is the most likely progenitor of the transient, its recent brightening in 2024 (reaching an absolute magnitude of -9) makes it an interesting candidate for followup.

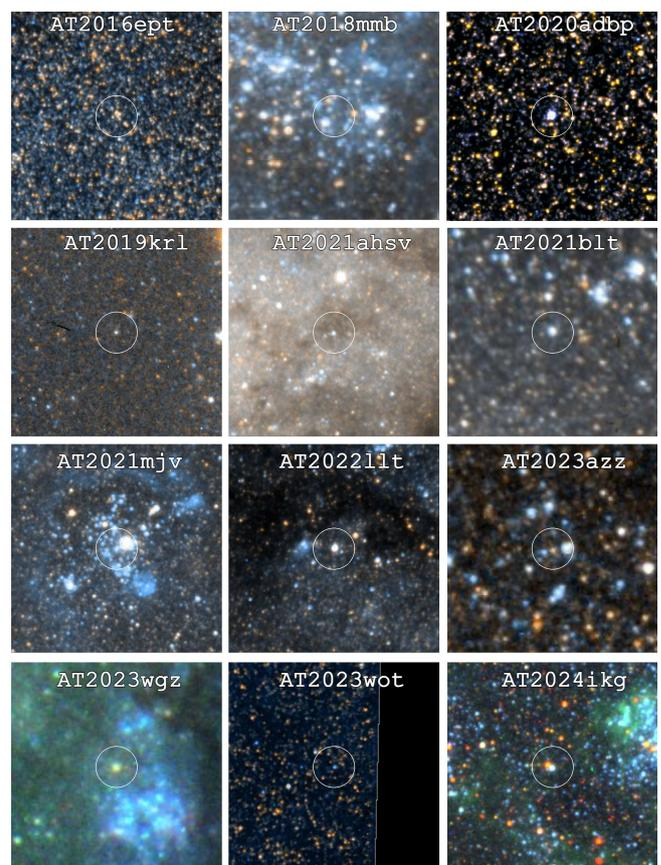


Fig. 13. HST cutouts of the 12 candidates resulting from our TNS cross-match. Images are $10''$ side-to-side, with a circle of $1''$ radius pinpointing the location of the YSG source. Adapted from HLA colour composites.

AT2019krl: this transient matches a YSG candidate with a separation below $0.1''$ and a stellar mass $\sim 10.3M_{\odot}$. Image inspection shows that the YSG is devoid of any bright source in its immediate vicinity. *AT2019krl* was spectroscopically classified as SN IIn or LBV outburst by The Astronomer’s Telegram, No. 12913. However, the absolute magnitude peak at -8.5 is several magnitudes fainter than most SN IIn. It was detected by HST at an absolute magnitude of -6 , translating to a ZAMS stellar mass of $\sim 10M_{\odot}$, less massive than most LBV. Still, their measured H_{α} line velocity (~ 2000 km/s) rules out a LRN-related mechanism.

AT2020adbp: this source matches a YSG in M31 observed by HST in January 2023, with $m_{F814W} = 18.7$. This observation occurred after the transient report on TNS, explaining the bright HST magnitude. There is no pre-brightening image available in the HST archive, which precludes the study of the progenitor. Source confusion is unlikely for this source having $CI = 1.1$ in both $F814W$ and $F475W$ filters. Followup of this source is encouraged.

AT2021ahsv: this transient matches a YSG candidate located at $0.19''$ with $M_{*} \sim 12M_{\odot}$. It is brighter than every close-by source. Standing in the middle of the Hertzsprung gap in the CMD, this candidate progenitor shows an interesting light curve with a slow brightening. Followup of this source is encouraged, as it has showed a steady brightening since 2020.

AT2021blt: this transient is located at $0.59''$ of a $\sim 11M_{\odot}$ YSG candidate, in the middle of the Hertzsprung gap in the CMD. With only 3 detections, no long-term evolution can be de-

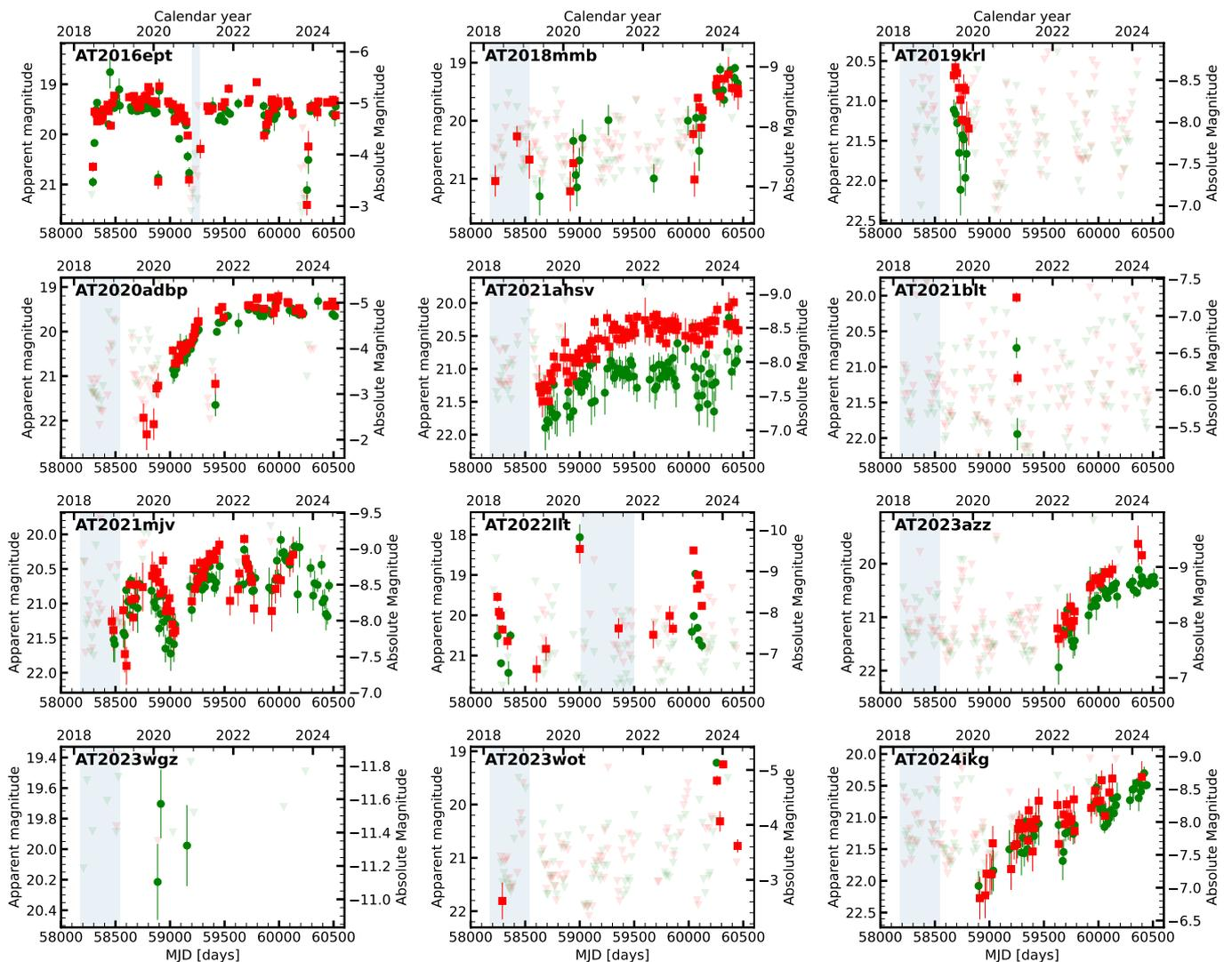


Fig. 14. ZTF forced photometry light curves of the 12 candidates resulting from our TNS cross-match. The blue areas indicate the period that was used to set the baseline flux at the location of these transients.

tected in its forced photometry light curve. Given the faint peak absolute magnitude, this transient may be a stellar outburst.

AT2021mjjv: this transient matches a $\sim 11M_{\odot}$ YSG with a separation of $0.21''$. This HST source is located in the Hertzsprung gap, towards the MS in the CMD. It is in a crowded area inside a stellar cluster. Source confusion is highly likely for this candidate, affecting its photometry ($CI = 1.8$). Given its apparent colour and starforming environment, we argue that this HST source is likely to be a MS star ($P_{\text{extin}} = 0.84$) selected as YSG because of source confusion. It may be a long-period variable as perhaps suggested by its light curve.

AT2022ilt: this transient matches a $> 20M_{\odot}$ YSG with a separation of $0.06''$. Although ZTF forced photometry does not reveal any long-term behavior, the ATLAS light curve shows a slow brightening of the source in recent years (Figure 16, top-middle panel). Image inspection shows that source confusion is unlikely for this source (also supported by its $CI=1.05$). Followup of this source is ongoing and encouraged.

AT2023azz: this transient is located at $0.51''$ from a $\sim 9.6M_{\odot}$ YSG candidate in M 101, according to its TNS coordinates. The ZTF coordinates, taking advantage of a large number of epochs, are even more precise and point to a separation of $0.2''$. Image

inspection reveals a faint, red source close to a brighter one (at $0.75''$). However, confusion may affect the photometry of this source, given the average CI of 1.4. Besides, its location on the CMD makes it also compatible with a RSG. Followup of this object is still encouraged.

AT2023wgz: this transient has a massive ($> 20M_{\odot}$) YSG counterpart at a $0.58''$ separation. Its photometry may be moderately affected by source confusion, with a CI of 1.4 in both *F814W* and *F555W* filters. Otherwise, it is not surrounded by any source of similar or greater luminosity. Its light curve shows only a few datapoints, with no detection since 2021.

AT2023wot: this source matches a $\sim 4M_{\odot}$ YSG in M 31 with a $0.58''$ separation. Although it is on the faint end of our M 31 selection, image inspection shows that it is not surrounded by any source of similar or greater luminosity, ruling out source confusion ($CI=1.13$). The Astronomer’s Telegram, No. 16319 suggest it to be a nova (Hornoch et al. 2023), which is in agreement with the absolute magnitude at peak of the forced photometry light curve (~ -5.3 , Figure 14). Such a rapid outburst also supports a nova-like behavior.

AT2024ikg: this recent transient is found to match a bright ($m_{F555W} = 21.73$), massive ($\sim 16M_{\odot}$) YSG candidate located

at 0.33" in M 101. Querying the HSCv3 detailed catalogue reveals that it was observed in Jan 2003 and Oct 2013, the only repeated filter being *F814W* and *F435W*. The source brightened from 22.06 to 21.65 (*F814W*) and 22.62 to 21.35 (*F435W*) in this interval. Inspection of the image reveals a bright RSG located just 0.25" away from the YSG, but at fainter magnitude ($m_{F555W} = 23.05$). Besides, the CI in both *F606W* and *F814W* is measured between 0.95 and 1.2 in both epochs, making source confusion unlikely. Followup of this object is encouraged.

4.3. Other precursor candidates

LRN precursors are expected to rise by only few magnitudes in several years (e.g. Blagorodnova et al. 2020). In this context, they may not meet the criteria to be reported to TNS (criteria may vary depending on the collaboration) until long after their detectability has begun. In order to retrieve them, we create a *Lasair*¹² (Smith et al. 2019) watchlist to match our YSG catalogue to all ZTF transient alerts with a matching radius of 0.6", and a *Lasair* filter to keep only objects with at least 2 positive detections ($ncand_{pg} \geq 2$).

To exclude variable stars, we inspected the ZTF light curve of each of the resulting 67 sources using the AlerCE broker (Förster et al. 2021), discarding all sources showing magnitudes in the past at levels brighter or similar to present levels. We used the ATLAS forced photometry tool¹³ on difference images to query candidate precursors and confirm the brightening trend on longer timescales. At this stage, we obtained nine precursor candidates consistently brightening over the last few years, including four objects previously analysed in Section 4.2 (AT2020adbp: ZTF20abhtvor, AT2021ahsv: ZTF20abbetli, AT2023azz: ZTF23aaazair, AT2024ikg: ZTF24aalfiak).

To obtain photometry for Southern candidates, we cross-matched YSG candidates to MeerLICHT and BlackGEM transients having at least 2 detections, at reasonable signal-to-noise ratio ($S/N > 6.5$) and high probability to be real (rather than bogus) $c_{class_real} > 0.8$. The matching radius used was 1". For BlackGEM and MeerLICHT, we obtained 10 and 33 matches, respectively. The large majority of them are variable stars with no clear brightening trend. For three of them, however, a brightening is identified and confirmed with ATLAS forced photometry: MLT28037995, in NGC 300, MLT15613547, in NGC 55, and MLT17180523 in NGC253, actually corresponding to AT2022ilt. The complete list of twelve (ZTF+MeerLICHT+BlackGEM) precursor candidates is detailed in Table 7. Their HST cutouts are presented in Figure 15 and their multi-survey light curves are shown in Figure 16. We fitted a slope to each light curve, in order to quantify the brightening trend. Slope values range between 2.1×10^{-4} and 1.2×10^{-3} mag day⁻¹, with an average error of 1.3×10^{-4} mag day⁻¹. In comparison, the brightening of the precursors of M31-LRN2015 and M101 OT2015-1 were respectively of 3 mags over 2 years and 1.5 mags over 6 years (Blagorodnova et al. 2017, 2020), corresponding to slopes of $\sim 4 \times 10^{-3}$ mag day⁻¹ and $\sim 7 \times 10^{-4}$ mag day⁻¹, respectively.

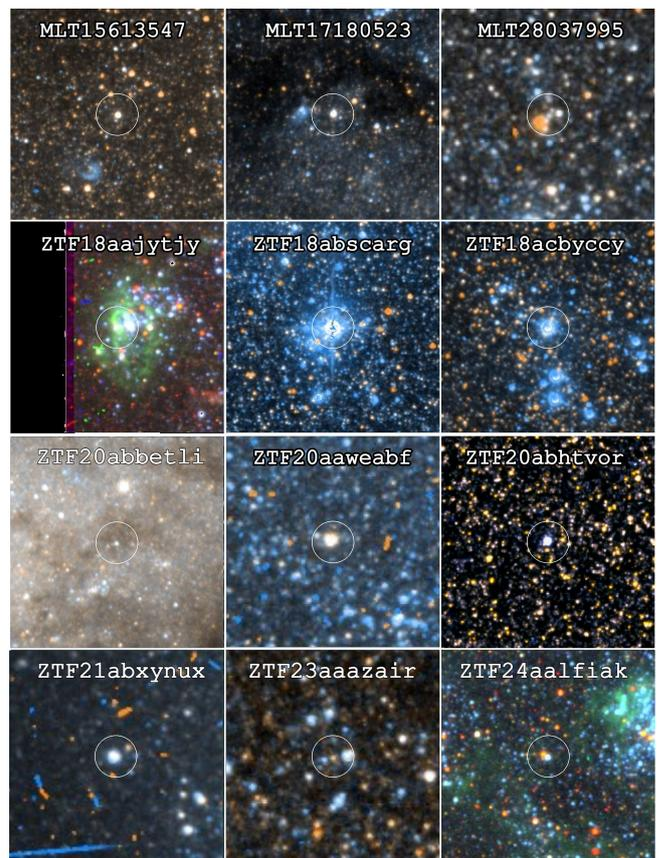


Fig. 15. HST cutouts of precursor candidates. Images are 10" side-to-side with a 1" radius circle centered on the HST position.

Galaxy	RA (deg)	Dec (deg)	m_{F814W} (mag)	Name	Sep. (")	Slope (mag/day)
M 31	11.15684	41.42050	21.3	ZTF18abscarg	0.43	-0.00123
M 31	11.04581	41.55485	17.8	ZTF18acbyccy	0.10	-0.00037
M 31	10.50249	41.14673	18.7	ZTF20abhtvor	0.01	-0.00043
M 101	210.70334	54.29897	20.8	ZTF18aaajytjy	0.32	-0.00037
M 101	210.75242	54.35229	23.2	ZTF23aaazair	0.22	-0.00036
M 101	210.61563	54.32963	21.0	ZTF24aalfiak	0.33	-0.00031
NGC 55	3.74938	-39.20321	18.7	MLT15613547	0.05	-0.00022
NGC 253	11.97423	-25.20828	19.5	MLT17180523	0.28	-0.00053
NGC 300	13.73000	-37.60991	23.0	MLT28037995	0.32	-0.00083
NGC 1560	68.21523	71.87764	18.6	ZTF21abxynux	0.19	-0.00054
NGC 6503	267.32443	70.15759	21.6	ZTF20abbetli	0.17	-0.00037
UGC 9240	216.18222	44.52105	19.0	ZTF20aaweabf	0.11	-0.00073

Table 7. Precursor candidates (sorted by galaxy name) identified in ZTF, MeerLICHT, or BlackGEM. The last column gives the slope of the best-fit linear trend to the ATLAS light curve.

5. Discussion

5.1. Comparison of our YSG candidates to spectroscopic samples

The literature provides a comprehensive representation of the brightest stars in M31 and M33, as well as their nature. To assess the validity of our method and further investigate the completeness and reliability of our YSG catalogue, we compare our sample to the spectroscopic YSG and RSG samples in M31 and M33 from Drout et al. (2009), Drout et al. (2012), Gordon et al. (2016), and Massey et al. (2016). In M31, within the CMD region used to select YSGs, Drout et al. (2009) identified 120 probable YSGs and 2772 foreground dwarfs. This identification was achieved by comparing the radial velocity obtained from their

¹² <https://lasair-ztf.lsst.ac.uk/>

¹³ <https://fallingstar-data.com/forcedphot/queue/>

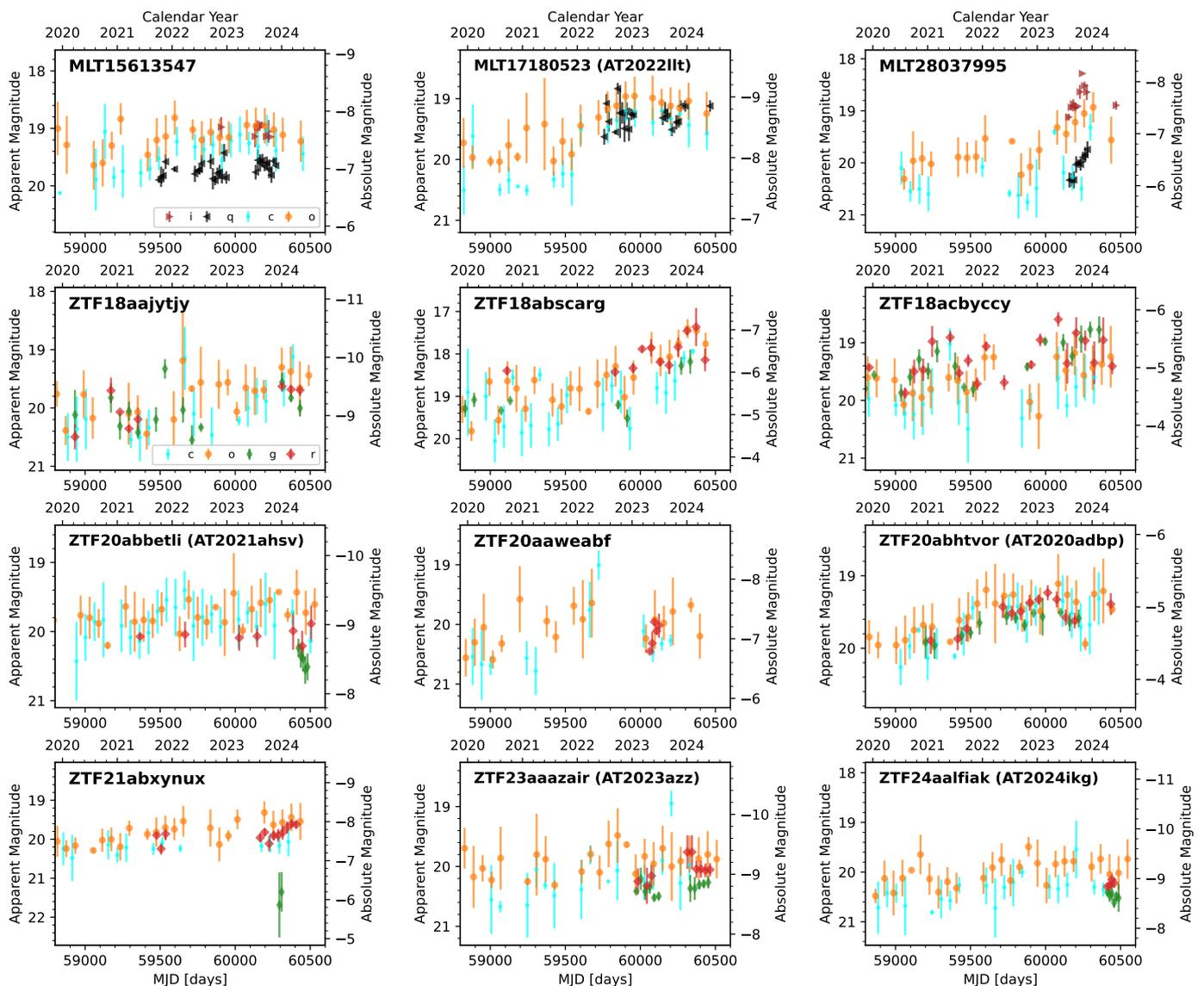


Fig. 16. ATLAS forced photometry light curves of the best 12 precursor candidates in ZTF, MeerLICHT and BlackGEM. ATLAS photometry is represented by orange and cyan circles (*o* and *c* bands), ZTF photometry by red and green diamonds (*r* and *g* bands) and MeerLICHT/BlackGEM photometry by black and brown triangles (*q* and *i* bands). ATLAS light curves were rebinned to 60-day bins, other surveys to 15-day bins.

spectra with the expected radial velocity at each position in M31, considering its peculiar velocity and rotation curve. Similarly, in M33, they identified 135 YSGs and 781 dwarfs (Drout et al. 2012). In a redder and less luminous region of the CMD, they identified 204 probable RSGs and 204 foreground dwarfs. The studies by Gordon et al. (2016) and Massey et al. (2016) refined these samples by identifying spectral types and members through their spectroscopic campaigns, including the extensive Local Group Galaxy Survey (LGGs, >1800 spectra).

Conversely, we used *Gaia* proper motions to eliminate foreground contaminants. To evaluate the effectiveness of this method, we crossmatched the samples from Drout (2009, 2012) and Gordon (2016) with *Gaia* DR3. For a minority of classified dwarfs, proper motion data is unavailable, constituting an anomaly. These stars are removed from the sample. The distribution of proper motion S/N is shown in Figure 17, categorised by the type of star they identified. The vast majority (98.5%) of foreground sources are correctly eliminated using *Gaia*'s proper motions. Additionally, 96.9% of the eliminated sources are in-

cluded foreground stars. *Gaia* proper motions prove to be an effective method for detecting foreground stars, comparable to spectroscopy or radial velocity methods.

Comparing the samples from Drout (2009, 2012) and Gordon (2016) to our sample, we obtain 931 associations (separation less than $0.6''$) for classified stars. The foreground contamination in this magnitude range is substantial, with approximately 89% of selected stars being foreground stars. After our cleaning, 96% of them are eliminated, and only 4% of M31's YSGs are removed. Therefore, the completeness of our sample is preserved, leaving only 23% residual contamination in this bright sample (typically $V < 19$). At fainter magnitudes, contamination is less significant. In M33, our method performs equally good. The pre-cleaning contamination is 56% (31 out of 56), and none of these 56 stars remain after filtering out high proper motions.

RSGs represent another type of contaminant in our sample. This is a direct consequence of the selected regions in the CMD, which include a portion of the RGB to avoid missing YSGs affected by extinction. In literature samples, the selection region

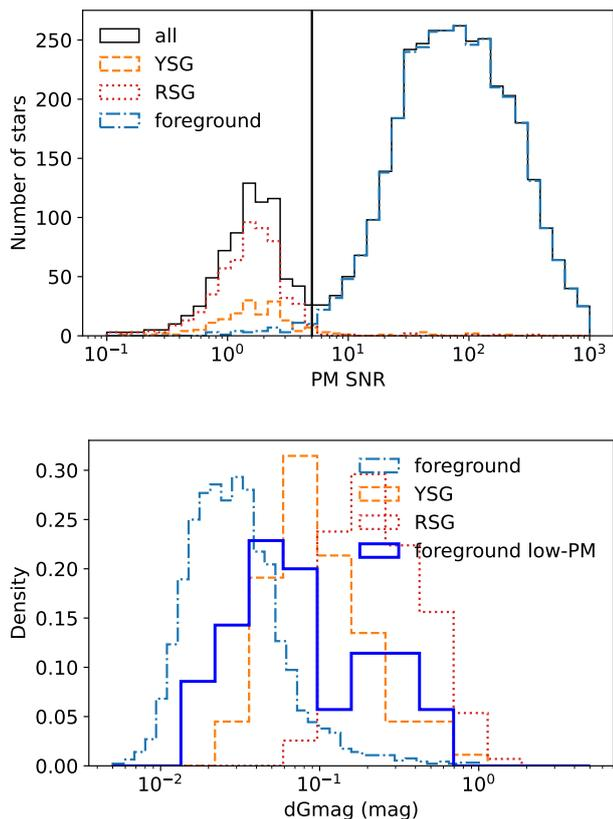


Fig. 17. (Top) Distribution of the *Gaia* DR3 proper motion signal-to-noise for M31 and M33 stars classified in the literature. (Bottom) Distribution of the variability indicator *dGmag* for M31 stars. The stars classified as foreground but with a low proper motion are shown in blue.

for RSGs is at a lower magnitude than for YSGs in the CMD, complicating the estimation of the fraction of RSG contaminants. At $V < 18.5$, however, our selection includes 44 YSGs and 14 RSGs, resulting in a contamination rate of 24%.

In addition to using proper motions, variability is an independent criterion that helps distinguishing a YSG from a foreground star. For example, massive YSGs have been known to vary erratically compared to low-mass dwarfs. The bottom panel of Figure 17 shows the distribution of the *Gaia*-measured *dGmag*, the difference between brightest and faintest *G*-band magnitude observed during the course of the survey. Interestingly, stars classified as foreground but with a low PM exhibit variability on average 6 times greater than those with proper motion data (average $dGmag=0.2$ instead of 0.033, Figure 17). This suggests a misclassification of these stars, which may be actual members of M31. To test this hypothesis, we model the distribution of *dGmag* as a sum of two distributions: one for high-PM sources identified as foreground, and one for low-PM sources identified as YSGs and RSGs. We can then estimate the contribution of YSGs and RSGs within low-PM foreground-classified stars. The fraction of these candidate members is $68 \pm 11\%$. This suggests that the residual contamination within low-PM stars with $V < 18.5$ is actually $\sim 8\%$ and not 23%. Furthermore, if our sample were to be used to identify progenitors of variable or transient events, the expected value of *dGmag* would be relatively large, further reducing the probability of association with a foreground source.

Finally, we can quantify the completeness of our YSG catalogue in different magnitude bins. Using for reference the sam-

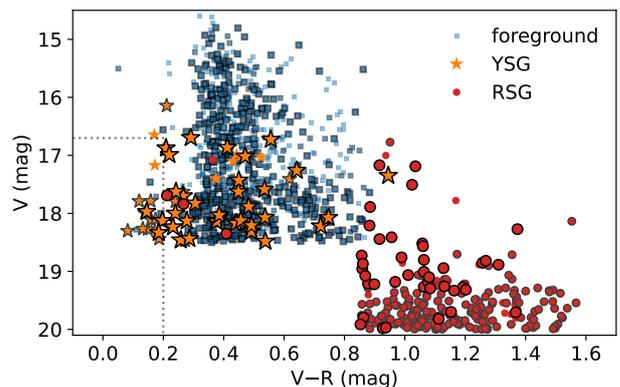


Fig. 18. CMD of M31 stars classified in the literature, using the photometry of Massey et al. 2016. Smaller markers without contour are stars present in HST footprint but not in HST catalogues, smaller markers with grey contour are stars in HST catalogues but not in our YSG selection, and larger markers with black contour are YSG selected candidates. The dotted lines highlight a region encompassing most of HST-detected YSG that are missed in our sample.

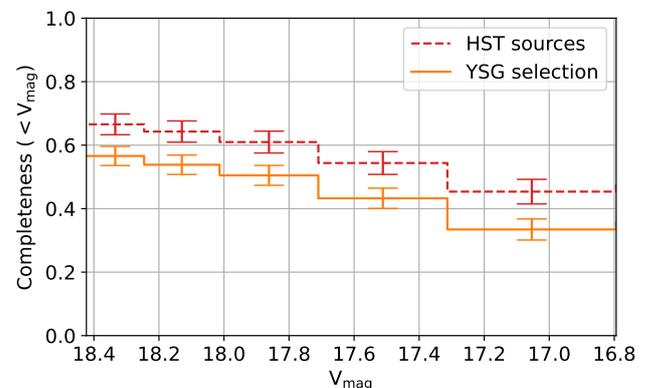


Fig. 19. Fraction of M31 YSG candidates from the literature recovered as HST sources and HST-selected YSG candidates, as a function of magnitude.

ples of YSG candidates in M31 from Drout et al. (2009) and Gordon et al. (2016) (see the corresponding CMD in Figure 18), and applying the same proper motion cut as done in our study, we obtain the completeness estimates shown in Figure 19. While the brightest stars are not always detected in third-party HST catalogues (and surveys other than HST are well-adapted to recover those), the fraction of recovered YSGs among recovered HST sources consistently remains around 80%. The lost fraction is primarily located in the dotted-line rectangle shown in Figure 18. This loss occurs because our conservative threshold, designed to exclude the main-sequence and some extinguished main-sequence stars, also omits YSGs in the bluer part of the CMD.

5.2. Impact of photometric uncertainties and source confusion

Source confusion is commonplace in crowded fields and can significantly bias the photometry of HST sources, leading to incorrect star classifications. This happens when two stars, such as a main-sequence star and a red giant, are in close angular proxim-

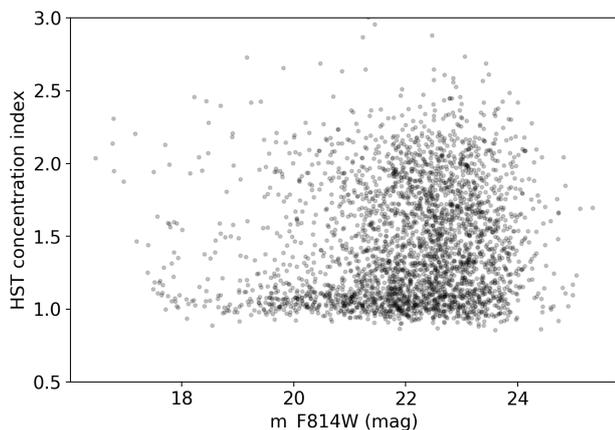


Fig. 20. HST photometric concentration index of YSG candidates as a function of their $F814W$ magnitude.

ity. Their combined light can be mistaken for a single star, such as a YSG, due to the blended colour and luminosity. This effect is another source of contamination affecting our YSG catalogue.

One method to quantify source confusion is by using the concentration index (CI), defined as the difference in magnitude between two apertures, typically a smaller aperture of $0.05''$ and a larger aperture of $0.15''$ (for ACS and WFC3/UVIS), normalised such that its distribution peaks at 1. Objects with CI values around 1.0 are likely to be stars, while those with significantly higher CI values are likely to be extended sources or the confusion of several stars. Figure 20 presents the distribution of YSG candidates in the $CI - m_{F814W}$ plane. At bright magnitudes, the CI is close to 1, showing that sources are point-like and source confusion is not significant. The faint sources are more numerous and thus denser on the sky, especially in distant galaxies. Therefore, they are more affected by source confusion and can have CI values close to 2.

Similarly, photometric uncertainties can bias the selection of YSGs in HST observations. These uncertainties arise from various sources, such as photon noise, background subtraction errors, and instrumental effects. When dealing with YSG candidates, identified based on their position in the CMD, even small errors in photometry can shift stars into or out of the YSG region. For example, in the NGC 4455 galaxy, an edge-on spiral galaxy located 7.3 Mpc away, observations were conducted using the $F814W$ filter for 1030 seconds. These parameters are close to the median values of our sample of galaxies with YSG candidates. When the colour-magnitude diagram is regenerated using magnitude values and errors modelled as a normal distribution, 9% of YSG candidates shift out of the selection region. Conversely, a similar number of previously unselected stars are shifted into the YSG selection region.

In this context, our conservative selection region helps to maintain a cleaner sample, although it may exclude some legitimate YSGs. Other sources of errors, such as uncertainties in stellar models, errors in extinction, distance, or metallicity of the host, may bias the selection region to a more significant extent.

5.3. Search for LRN Progenitors and Precursors with LSST

In a recent paper, Strotjohann et al. (2024) explore the potential for identifying progenitor stars of core-collapse supernovae using data from ground-based wide-field surveys such as ZTF and LSST. Due to challenges like crowding and atmospheric blur-

ring, identifying these progenitor stars in pre-explosion images is difficult. Instead, the study suggests combining numerous pre- and post-supernova images to detect the disappearance of progenitor stars. As a proof of concept, the authors implemented this approach using ZTF data. Despite analysing hundreds of images and achieving limiting magnitudes of approximately 23 in the g and r bands, no progenitor stars or long-lived outbursts were detected for 29 supernovae within a redshift of $z \leq 0.01$. The sensitivity limits achieved were several magnitudes less than those in previously detected progenitors.

Conversely, the study projects that LSST, over its 10-year survey, could detect around 50 red supergiant progenitors and several yellow and blue supergiants. It estimates that progenitors of Type Ic supernovae would be detectable if they are brighter than -4.0 magnitudes in the LSST i band, respectively. Given their similar spectral type (A5) compared to YSGs, we assume a similar performance for YSG detection: we therefore expect that 77% of our YSG sample will be redetected by LSST, for sources having $M_{F814W} < -4$ (or $M_* > 6M_{\odot}$, Figure 9). This will provide exquisite variability constraints for sources of $r < 23$, allowing us to identify new LRN precursors, given LSST repeated observations and the long timescales of these events. Furthermore, LSST can expand the progenitor sample for the 1235 galaxies within 20 Mpc and at $Dec < 30^{\circ}$ that are not covered by deep multiband HST exposures. In particular, it will cover more than 1200 massive galaxies ($M_B < -14$ to select starforming hosts), where LRNe are most likely, and whose YSGs comprise 96% of our sample. Assuming the same distance distribution of YSG candidates as the one in this study, this represents a 130% increase of our $M_* > 6M_{\odot}$ sample. It is important to note that some progenitors detected only a few years before the LRN are likely already undergoing mass transfer and can be considered precursors (this is the case of e.g. AT2021blu, imaged both 15 years and 2 years prior to the transient, showing a 1-mag brightening between these two epochs Pastorello et al. 2023).

The rate of LRNe in the luminosity range $-16 \leq M_r \leq -11$ mag was recently constrained to $7.8_{-3.7}^{+6.5} \times 10^{-5} \text{ Mpc}^{-3} \text{ yr}^{-1}$ (Karambelkar et al. 2023), comparable to the core-collapse SN rate (Perley et al. 2020). However, LRNe are about three magnitudes fainter, and Karambelkar et al. (2023) suggest a luminosity function in the form $dN/dL \propto L^{-2.5}$. At magnitude $r < 18.5$, we thus expect LSST to detect about 50 LRNe (i.e. 1.7% of the 3300 expected bright core-collapse SNe, Strotjohann et al. 2024) over its 10-year survey.

Strotjohann et al. (2024) also postulate how LSST will detect more than a thousand pre-supernova outbursts, depending on their brightness and duration. In the case of LRNe precursors, a system brightening from -1 to -4 mag in absolute r -band magnitude (similar to the precursor of M31-LRN2015) would be detected in a single LSST exposure up to a distance of 5 Mpc (not taking into account the effects of the luminous background from the galaxy). This distance limit becomes 20 Mpc when using the final survey LSST r -band sensitivity. Considering the host galaxy's brightness, late-time precursors or those from massive stars, with $M_r < -6$ (Blagorodnova et al. 2020, Figures 14, 16) would have a 6% probability of detection by LSST (Strotjohann et al. 2024). If half LRNe have such a precursor, given their volumetric rate, one can expect about 100 new precursor detections in the era of LSST. The rate, luminosity function, and timing of LRN precursors will be measurable using this large dataset. This might contribute to revealing their intrinsic mechanisms.

Overall, the cadence of LSST, its multi-band coverage, along with the depth of the survey, allows for the detection of progenitors, years-long faint precursors and variability patterns that pre-

cede LRN events. Systematic cataloging and data mining techniques will be crucial in identifying these specific observational signatures within LSST vast datasets. An approach based on the systematic use of archival data and the prediction of future variability using various light-curve analysis techniques is under study (Tranin et al., in prep.).

6. Conclusion

In this study, we use HST imaging of nearby galaxies to find possible LRN progenitors and precursors, making it possible to predict their outburst and rapidly identify new transients matching the position of a candidate YSG. We retrieve the catalogues of HST sources and their photometry for 369 galaxies with distances closer than 20 Mpc, using different public databases. After building colour magnitude diagrams for each galaxy, we select the Hertzsprung gap stars using MIST stellar evolution tracks, coupled with a statistical representation of the CMD. Foreground contaminants were mostly removed using *Gaia* proper motions, and the rest of foreground contaminants was quantified using the TRILEGAL simulations of the Milky Way stellar content. The previous spectroscopic identification of foreground stars within the Hertzsprung gap of M31 and M33 showed excellent agreement with our method. Additionally, we constrained the number of contaminants resulting from internal extinction to less than 20% of the sample and quantified this for each source. The use of MIST stellar evolution tracks and a meticulous filtering process to exclude contaminants proved crucial in accurately identifying candidates.

Our study identified 233,336 yellow supergiant candidates in 355 galaxies, a significant increase over previous research. The resulting sample of candidates was cross-matched with the TNS and the ongoing surveys ZTF, BlackGEM and MeerLICHT. Candidates exhibiting outstanding variability were identified and analysed. In particular, we identified 12 precursor candidates based on their consistent brightening over the past few years. Their spectroscopic followup and identification will be the subject of an upcoming work.

The YSG catalogue resulting from this study will be released at the time of publication of this article, together with the pipeline. The Python scripts used to retrieve and analyse HST data are made publicly available at the following address: <https://github.com/htranin/LRNsearch>. The insights gained from this catalogue can inform future models of stellar evolution and enhance our ability to predict and study rare transient events. This work advances our capabilities to understand yellow supergiants and their role as progenitors and precursors to luminous red novae, filling a gap in previous studies. LSST will be a game changer in the quest for LRNe and their progenitors and precursors: we estimate that the 10-year survey will more than double the number of detected extragalactic YSGs within 20 Mpc, and provide excellent variability constraints for sources of magnitude $r < 23$. Notably, based on the rate of previous extragalactic LRNe, we expect about 100 LRN precursors to be discovered over the course of LSST, and about 50 bright $r < 18.5$ LRNe. Future research should focus on continuous monitoring of brightening YSG candidates to capture and analyse transient episodes as they occur. We emphasize the importance of closely monitoring these future transients having YSG progenitor, to ensure the identification and study of luminous red novae events and other rare transients.

Acknowledgements. H. T. and N. B. acknowledge to be funded by the European Union (ERC, CET-3PO, 101042610). Views and opinions expressed are however those of the author(s) only and do not necessarily reflect those of the

European Union or the European Research Council Executive Agency. Neither the European Union nor the granting authority can be held responsible for them. We acknowledge the extensive use of the MAST database to conduct this study. Based on observations with the MeerLICHT telescope. MeerLICHT is built and run by a consortium consisting of Radboud University, the University of Cape Town, the South African Astronomical Observatory, the University of Oxford, the University of Manchester and the University of Amsterdam. MeerLICHT is hosted by SAAO. Based on observations with the BlackGEM telescopes. BlackGEM is built and run by a consortium consisting of Radboud University, the Netherlands Research School for Astronomy (NOVA), and KU Leuven with additional support from Armagh Observatory and Planetarium, Durham University, Hamburg Observatory, Hebrew University, Las Cumbres Observatory, Tel Aviv University, Texas Tech University, Technical University of Denmark, University of California Davis, the University of Barcelona, the University of Manchester, University of Potsdam, the University of Valparaiso, the University of Warwick, and Weizmann Institute of science. BlackGEM is hosted and supported by ESO.

References

- Addison, H., Blagorodnova, N., Groot, P. J., et al. 2022, MNRAS, 517, 1884
 Aryan, A., Pandey, S. B., Zheng, W., et al. 2021, MNRAS, 505, 2530
 Asplund, M., Grevesse, N., Sauval, A. J., & Scott, P. 2009, ARA&A, 47, 481
 Astropy Collaboration, Robitaille, T. P., Tollerud, E. J., et al. 2013, A&A, 558, A33
 Bellm, E. C., Kulkarni, S. R., Graham, M. J., et al. 2019, PASP, 131, 018002
 Bertin, E. & Arnouts, S. 1996, A&AS, 117, 393
 Blagorodnova, N., Karambelkar, V., Adams, S. M., et al. 2020, MNRAS, 496, 5503
 Blagorodnova, N., Kléncki, J., Pejcha, O., et al. 2021, A&A, 653, A134
 Blagorodnova, N., Kotak, R., Polshaw, J., et al. 2017, ApJ, 834, 107
 Bloemen, S., Groot, P., Woudt, P., et al. 2016, in Society of Photo-Optical Instrumentation Engineers (SPIE) Conference Series, Vol. 9906, Ground-based and Airborne Telescopes VI, ed. H. J. Hall, R. Gilmozzi, & H. K. Marshall, 990664
 Cai, Y. Z., Pastorello, A., Fraser, M., et al. 2022, A&A, 667, A4
 Choi, J., Dotter, A., Conroy, C., et al. 2016, ApJ, 823, 102
 Dal Tio, P., Pastorelli, G., Mazzi, A., et al. 2022, ApJS, 262, 22
 Delchambre, L., Bailer-Jones, C. A. L., Bellas-Velidis, I., et al. 2023, A&A, 674, A31
 Dotter, A. 2016, ApJS, 222, 8
 Drout, M. R., Massey, P., & Meynet, G. 2012, ApJ, 750, 97
 Drout, M. R., Massey, P., Meynet, G., Tokarz, S., & Caldwell, N. 2009, ApJ, 703, 441
 Flesch, E. W. 2021, arXiv e-prints, arXiv:2105.12985
 Förster, F., Cabrera-Vives, G., Castillo-Navarrete, E., et al. 2021, AJ, 161, 242
 Gaia Collaboration, Bailer-Jones, C. A. L., Teyssier, D., et al. 2023a, A&A, 674, A41
 Gaia Collaboration, Brown, A. G. A., Vallenari, A., et al. 2018, A&A, 616, A1
 Gaia Collaboration, Brown, A. G. A., Vallenari, A., et al. 2021, A&A, 649, A1
 Gaia Collaboration, Vallenari, A., Brown, A. G. A., et al. 2023b, A&A, 674, A1
 Georgy, C. 2012, A&A, 538, L8
 Ginsburg, A., Sipőcz, B. M., Brasseur, C. E., et al. 2019, AJ, 157, 98
 Girardi, L., Groenewegen, M. A. T., Hatziminaoglou, E., & da Costa, L. 2005, A&A, 436, 895
 Gordon, M. S., Humphreys, R. M., & Jones, T. J. 2016, ApJ, 825, 50
 Groot, P., Bloemen, S., & Jonker, P. 2019, in The La Silla Observatory - From the Inauguration to the Future, 33
 Groot, P. J., Bloemen, S., Vreeswijk, P., et al. 2024, arXiv e-prints, arXiv:2405.18923
 Hornoch, K., Shafter, A. W., Kucakova, H., Yosuf, I., & Luo, A. 2023, The Astronomer's Telegram, 16319, 1
 Jacobson-Galán, W. V., Davis, K. W., Kilpatrick, C. D., et al. 2024, arXiv e-prints, arXiv:2404.19006
 Justham, S., Podsiadlowski, P., & Vink, J. S. 2014, ApJ, 796, 121
 Kankare, E., Kotak, R., Pastorello, A., et al. 2015, A&A, 581, L4
 Karambelkar, V. R., Kasliwal, M. M., Blagorodnova, N., et al. 2023, ApJ, 948, 137
 Kochanek, C. S., Adams, S. M., & Belczynski, K. 2014, MNRAS, 443, 1319
 Kovlakas, K., Zezas, A., Andrews, J. J., et al. 2021, MNRAS, 506, 1896
 Kraft, R. P. 1966, ApJ, 144, 1008
 Lasker, B. M., Doggett, J., McLean, B., et al. 1996, in Astronomical Society of the Pacific Conference Series, Vol. 101, Astronomical Data Analysis Software and Systems V, ed. G. H. Jacoby & J. Barnes, 88
 MacLeod, M., De, K., & Loeb, A. 2022, ApJ, 937, 96
 MacLeod, M., Macias, P., Ramirez-Ruiz, E., et al. 2017, ApJ, 835, 282
 Marchant, P. & Bodensteiner, J. 2023, arXiv e-prints, arXiv:2311.01865
 Martini, P., Wagner, R. M., Tomanev, A., et al. 1999, AJ, 118, 1034

- Masci, F. J., Laher, R. R., Rusholme, B., et al. 2023, arXiv e-prints, arXiv:2305.16279
- Massey, P., Neugent, K. F., & Smart, B. M. 2016, AJ, 152, 62
- Massey, P., Waterhouse, E., & DeGioia-Eastwood, K. 2000, AJ, 119, 2214
- Moe, M. & Di Stefano, R. 2017, ApJS, 230, 15
- Mora, M. D., Larsen, S. S., & Kissler-Patig, M. 2007, A&A, 464, 495
- Neugent, K. F., Massey, P., Skiff, B., et al. 2010, ApJ, 719, 1784
- Neustadt, J. M. M., Kochanek, C. S., Stanek, K. Z., et al. 2021, MNRAS, 508, 516
- Paczynski, B. 1976, in Structure and Evolution of Close Binary Systems, ed. P. Eggleton, S. Mitton, & J. Whelan, Vol. 73, 75
- Pastorello, A., Fraser, M., Valerin, G., et al. 2021a, A&A, 646, A119
- Pastorello, A., Mason, E., Taubenberger, S., et al. 2019, A&A, 630, A75
- Pastorello, A., Valerin, G., Fraser, M., et al. 2021b, A&A, 647, A93
- Pastorello, A., Valerin, G., Fraser, M., et al. 2023, A&A, 671, A158
- Paturel, G., Petit, C., Prugniel, P., et al. 2003, A&A, 412, 45
- Paxton, B., Bildsten, L., Dotter, A., et al. 2011, ApJS, 192, 3
- Perley, D. A., Fremling, C., Sollerman, J., et al. 2020, ApJ, 904, 35
- Pessi, T., Cartier, R., Hueichapan, E., et al. 2024, arXiv e-prints, arXiv:2405.02274
- Pilyugin, L. S., Vilchez, J. M., & Contini, T. 2004, A&A, 425, 849
- Reig, P., Tzouvanou, A., & Pantoulas, V. 2022, The Astronomer's Telegram, 15612, 1
- Smartt, S. J. 2015, PASA, 32, e016
- Smith, K. W., Williams, R. D., Young, D. R., et al. 2019, Research Notes of the American Astronomical Society, 3, 26
- Smith, N., Andrews, J. E., Van Dyk, S. D., et al. 2016a, MNRAS, 458, 950
- Smith, N., Andrews, J. E., Van Dyk, S. D., et al. 2016b, MNRAS, 458, 950
- Stetson, P. B. 1987, PASP, 99, 191
- Strotjohann, N. L., Ofek, E. O., Gal-Yam, A., et al. 2024, ApJ, 960, 72
- Teffs, J. J., Prentice, S. J., Mazzali, P. A., & Ashall, C. 2021, MNRAS, 502, 3829
- Tonry, J. L., Denneau, L., Heinze, A. N., et al. 2018, PASP, 130, 064505
- Tran, H. D., Burger, M., & Hack, W. 2020, in Astronomical Society of the Pacific Conference Series, Vol. 527, Astronomical Data Analysis Software and Systems XXIX, ed. R. Pizzo, E. R. Deul, J. D. Mol, J. de Plaa, & H. Verkoeter, 587
- Tylenda, R., Hajduk, M., Kamiński, T., et al. 2011, A&A, 528, A114
- Tylenda, R. & Soker, N. 2006, A&A, 451, 223
- Van Dyk, S. D., Zheng, W., Brink, T. G., et al. 2018, ApJ, 860, 90
- Whitmore, B. C., Allam, S. S., Budavári, T., et al. 2016, AJ, 151, 134
- Williams, S. C., Darnley, M. J., Bode, M. F., & Steele, I. A. 2015, ApJ, 805, L18

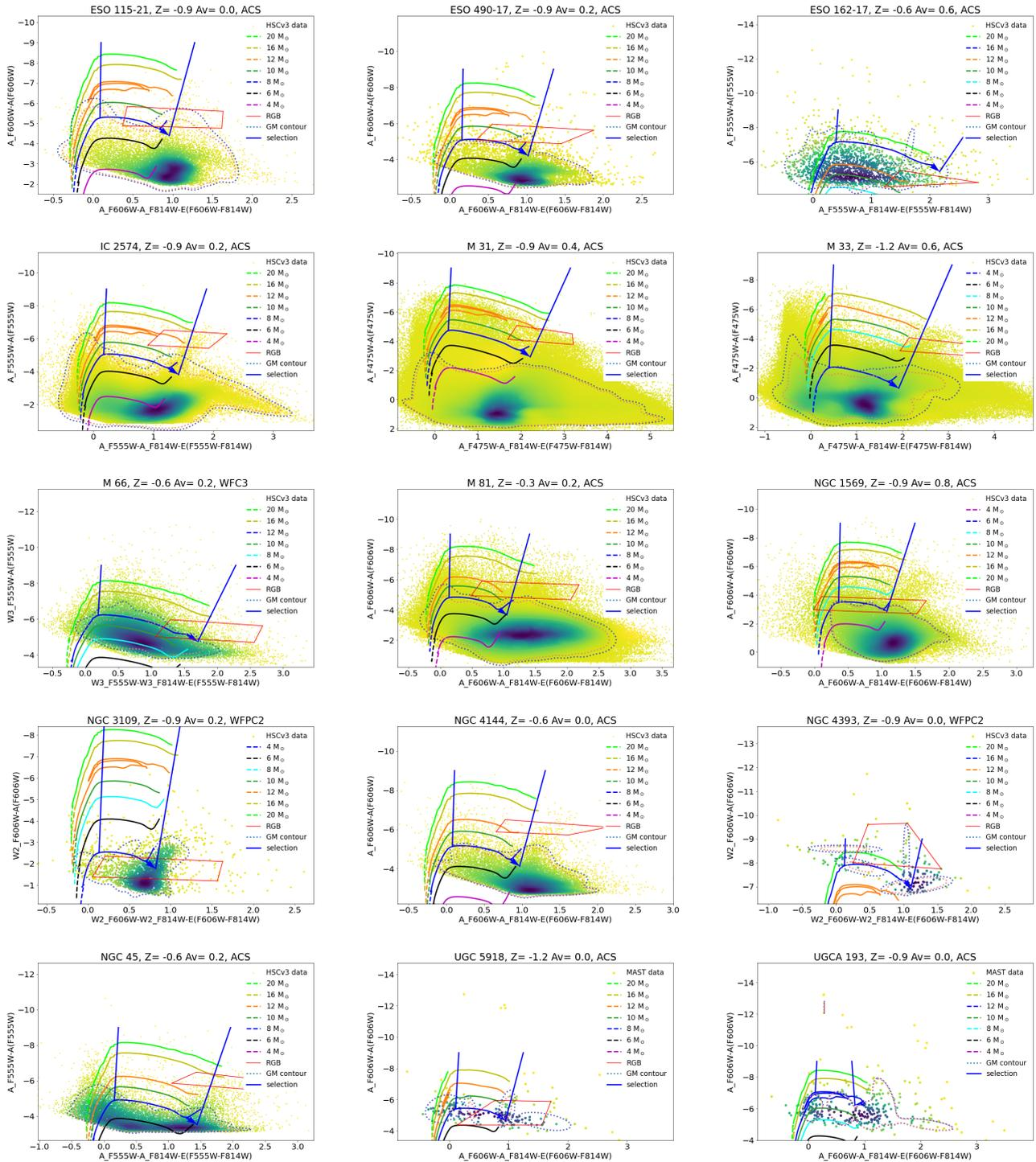


Fig. A.1. Representative sample of CMDs analysed in this study. The blue MIST track corresponds to the reference stellar mass at which YSG observation completeness is ensured.

Appendix A: Example of CMDs

Figure A.1 presents a representative subset of CMDs analysed in this study. The selection area of YSG candidates is shown by solid blue lines.